RESEARCH REPORT

VTT-R-09735-10

Magnetite dissolution and deposition in NPP secondary circuit

Authors: Mikko Vepsäläinen, Timo Saario

Confidentiality: Public

Report's title	
Magnetite dissolution and deposition in NPP secondary circuit	
Customer, contact person, address SAFIR2010, Finnish national research program on NPP safety 2007-2010	Order reference
Project name Monitoring of the Structural Integrity of Reactor Circuit	Project number/Short name 41632 / RAKEMON
Author(s) Mikko Vepsäläinen, Timo Saario	Pages 44/
Keywords Nuclear power plant, secondary circuit, magnetite dissolution, magnetite deposition	Report identification code VTT-R-09735-10

Summary

This work was a part of SAFIR2010, Finnish national research program on NPP safety 2007-2010. The goal of this review was to gather information from various sources to gain understanding of the present situation of the research related to magnetite dissolution and deposition.

Magnetite dissolution and deposition are major problems in many nuclear power plants (NPP). High removal rate of protecting oxide layer decreases the operating life of the equipment and causes dangerous situations, which can lead to casualties and major financial losses. Mechanism of flow accelerated corrosion (FAC) is generally well-understood and there are several models and software which predict FAC rate with good accuracy. FAC can be considered as an extension of a general corrosion process, where dissolution of the surface oxide is accelerated due to enhanced mass transfer of soluble species from the surface. The main parameters having influence on the magnetite dissolution rate are: concentrations of oxidants and reductants, electrochemical potential, temperature, pH, material properties (alloying elements) and hydrodynamic factors.

The factors affecting magnetite deposition are basically less well understood. Theories of magnetite deposition can be divided into models describing the deposition of soluble iron and models describing the deposition of magnetite particles. Especially the factors affecting the attachment of the particles should be further studied.

Confidentiality	Public

Espoo 2.12.2010

Written by	Reviewed by	Accepted by
Mikko Vepsäläinen Research Scientist	Ari Koskinen Team Leader	Pentti Kauppinen Technology Manager

VTT's contact address

Distribution (customer and VTT)
SAFIR2010

Preface

This literature review has been made at VTT Espoo office during the year 2010. This research was part of SAFIR2010, Finnish national research program on NPP safety 2007-2010.

Espoo 2.12.2010

Authors

Contents

1 Introduction

Magnetite dissolution and deposition are major problems in many nuclear power plants (NPP). High removal rate of the protecting oxide layer decreases the operating life of the equipment and causes dangerous situations which can lead to casualties and major financial losses. Due to flow accelerated corrosion (FAC) four workers were killed at the Surry nuclear plant and financial losses were tens of millions of dollars. This led to a coordinated approach of inspection and non-destructive evaluation at the plants. However, subsequently there have been several serious accidents that have been caused by FAC, such as incidents at Pleasant Prairie, Mihama and Iatan. Magnetite removal, and hence iron dissolution, are also the main sources of the iron-based material which causes deposition in the secondary cycle.

FAC has been studied for over 40 years at several locations around the world and the mechanism and parameters influencing it are quite well known. There are numerous studies made after first fatalities at the mid 1980's when seriousness of FAC was realized. Terms "flow-assisted corrosion" and "erosion-corrosion" have been used earlier to define FAC and related research can be found using these keywords.

Magnetite deposition causes steam generator fouling, which is believed to be a root or contributing cause for several SG degradation modes. There are models which can be used to estimate the fouling due to dissolved or particulate material. However, magnetite deposition is basically less understood than magnetite dissolution and especially FAC. This is easily understood because FAC can cause life-threatening situations whereas magnetite deposition causes degraded efficiency and financial losses.

2 Goal

In the present literature review, the models describing magnetite dissolution and deposition in NPP secondary cycles are described. Magnetite dissolution studies are mainly related to FAC and therefore mechanisms of FAC are gone through in detail together with major parameters influencing the FAC rate. Models describing the magnetite deposition are reviewed at the end of this report.

The goal of this review is to gather information from various sources in order to increase our understanding of the present situation of magnetite dissolution and deposition related investigations. Special focus is on latest research results found from literature. Results of the research work made at other industrial sectors are also reviewed in this report when they have important aspects considering magnetite dissolution and deposition.

3 Magnetite dissolution

3.1 Mechanism of flow accelerated corrosion

FAC is often mislabeled as erosion-corrosion. The term erosion-corrosion includes several erosion and corrosion mechanisms, including purely mechanical damage and flow accelerated corrosion where oxide film is thinned due to high flow and not by mechanical stresses. Different mechanisms of erosion-corrosion are listed in Table 1.

Table 1: Spectrum of erosion-corrosion processes [1].

Dissolution dominant
Flow thins protective film to equilibrium thickness which is a function of both mass transfer rate and growth kinetics.
Erosion corrosion rate is controlled by the dissolution of the protective film.
Film is locally removed by dissolution, fluid induced stress or particler bubble impact: but it can repassivate. Erosion corrosion rate is a function of the frequency of film removal, bare metal dissolution rate and subsequent repassivation rate
Film is removed and does not reform. Erosion corrosion rate is the rate the bare metal can dissolve.
Film is removed and underlying metal surface is mechanically damaged which contributes to overall metal loss, i.e., erosion corrosion rate is equal to bare metal dissolution rate plus possibly synergistic effect of mechanical damage.
Film is removed and mechanical damage to underlying metal is the dominant damage mechanism
Mechanical damage dominant

After extensive research in the past two decades, the general mechanism of FAC seems to be well understood. FAC is a degradation process that affects carbon steel and in less extent low-alloy steels [2]. During the FAC process, the protective magnetite surface layer dissolves into the water stream or wet steam. High flow rates accelerate the removal of the oxide layer and the migration of the dissolved iron ions from the surface. After sufficient wall thinning severe incidents, such as pipe or tube bursts, can occur. The wall-thinning rates can be as high as 3 mm/year [3].

FAC is an extension of general corrosion process of carbon steel in stagnant water. The major difference is the effect of water flow to the oxide-water interface. FAC can be divided into few processes that occur at the iron-magnetite interface, in the oxide layer and at the oxide-water interface [3-5]. These FAC processes are depicted in Figure 1:

1. Generation of soluble ferrous ions at the oxide-water interface. Ferrous ions are produced either as a result of metal oxidation at the iron-magnetite interface (Eq. 2) and transport of ferrous ions through the oxide into the

water flow, or when the magnetite oxide layer itself is reduced and dissolved.

2. Transportation of ferrous ions into the water stream across the fluid boundary layer. The concentration of the soluble ferrous ions in the water stream is significantly lower than the concentration at the oxide-water interface. Corrosion rate increases when flow at the oxide-water interface increases and accelerates migration of the dissolved ions away from the surface.

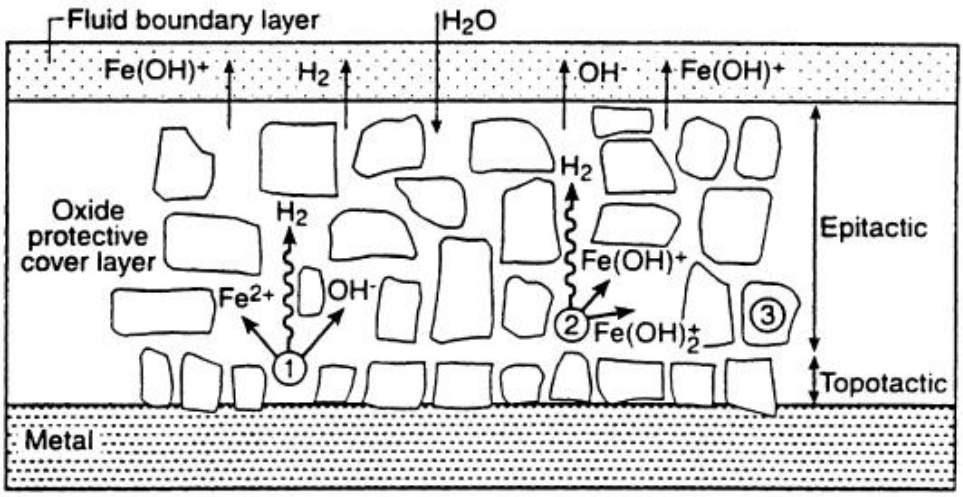

Figure 1: Schematic picture of the magnetite layer formed on the iron-based material surface during the operation with deoxygenated all-volatile treatment (AVT) in reducing conditions [3].

Formation of soluble ferrous ions occurs at the iron-oxide interface through the electrochemical reactions (anodic Eq. 1 and cathodic Eq. 2).

$$Fe \rightarrow Fe^{2+} + 2e^{-} \quad (1)$$

$$2H_2O + 2e^{-} \rightarrow 2OH^{-} + H_2 \quad (2)$$

The ferrous ions and ferrous hydroxide are at equilibrium according to Eq 3.

$$Fe^{2+} + nOH^{-} \leftrightarrow Fe(OH)_n^{(2-n)} \quad (3)$$

The reductive dissolution of magnetite is controlled by oxidation-reduction potential (ORP) of the water and is promoted by the presence of hydrogen. More reducing feedwater leads to faster dissolution through the reduction of magnetite. This is described in more detailed in chapter 3.1.1.

FAC is considered to be a steady-state corrosion process which exhibits linear corrosion kinetics [6]. The reduced magnetite layer at the oxide-water interface is replaced with a new magnetite layer of the same thickness at the metal-oxide interface. Non-linear initiation period of the FAC rate can occur when the surface has preformed magnetite layer. However, longer exposure eventually leads to

linear corrosion rate with the time. The rate of dissolution (through the reduction reaction) at the oxide-water interface can be described as a first-order reaction that is depicted in Eq. 4.

$$V_C = K(C_{eq} - C) \quad (4)$$

Where K is the reaction rate constant, C_{eq} is the soluble ferrous ion concentration at the equilibrium with the magnetite and C is the soluble ion concentration at the oxide-water interface. As stated earlier, soluble ferrous ions are also produced at the metal-oxide interface and transported by diffusion through the oxide layer. This represents a part of the total ferrous ion production. Remy et al. assumed that total corrosion rate is equal to twice the rate of ferrous ions produced by the reduction of the magnetite layer (Eq. 5) [6]. The concentration of the soluble ferrous ions at the equilibrium with the magnetite depends on pH of the water, hydrogen pressure and temperature.

$$V_{TC} = 2K(C_{eq} - C) \quad (5)$$

Transfer of the ferrous ions to the bulk water can be modeled as convective transport phenomenon according to Eq. 6 [6].

$$F_{IF} = K_m(C - C_0) \quad (6)$$

Where K_m is the mass transfer constant and C_0 is the ferrous ion concentration at the bulk flow. At stationary conditions, F_{IF} and V_{TC} are equal and total dissolution rate can be described by Eq. 7.

$$V_{TC} = \frac{2KK_m(C_{eq} - C_0)}{K_m + 2K} \quad (7)$$

Bouchacourt et al. have obtained results which show that FAC rate is proportional to the magnetite solubility and the mass transfer rate in alkaline pH range when the mass transfer coefficient $K_m \leq 1$ mm/s (Re ≤ 150000) [8, 9]. Eq. 7 describes the correlation between the FAC rate and the mass transfer. They have concluded that the reaction kinetics of the magnetite dissolution is faster than the mass transfer ($K >> K_m$, i.e. $K_m/K \approx 0$) and thus FAC is a convective diffusion controlled process. Ferrous ion concentration at the bulk flow, C_o, can usually be estimated to be zero and therefore, Eq. 7 simplifies to Eq. 8.

$$V_{TC} = K_m C_{eq} \quad (8)$$

When K > 1 mm/s (Re > 150000) a deviation from the linear correlation of the mass transfer coefficient and FAC rate is obtained.

According to results of Bouchacourt, FAC rate is controlled by the parameters that affect magnetite solubility and mass transfer [8, 9]. Hydrodynamic conditions have significant influence on the FAC rate because dissolution rate of the surface oxide is related to the mass transfer of the soluble species from the surface [4, 6]. Hydrodynamic factors are gone through in detail in section 3.2.5. Temperature

and at-temperature pH have influence to the solubility of the magnetite and ferrous hydroxide. These are gone though in sections 3.2.3 and 3.2.3. ORP and concentration of oxidizing and reducing chemical species influence the composition of the oxide layer. Effect of ORP and hydrazine are described in section 3.2.1. Alloying metals can affect the solubility of the oxide layer, which is discusses in section 3.2.4.

MIT has developed a model which includes the diffusion of the ferrous ions through the oxide layer and takes also into account the oxide porosity and thickness [7]. When ferrous ion concentration at the bulk flow is assumed zero (C_0 = 0) FAC rate can be described by Eq. 9.

$$V_{TC}(MIT) = \frac{C_{eq}\theta}{\frac{1}{K} + 0{,}5\left(\frac{1}{K_m} + \frac{\delta}{D}\right)} \qquad (9)$$

In Eq. 9 θ is the oxide porosity and δ is the oxide thickness. Assuming $\delta / D << 1/ K_m$, and that porosity is 50% (i.e. $\theta = 0.5$, eq. (9) reduces to eq. (8).

3.1.1 Magnetite solubility

Solubility is a thermodynamical concept which refers to maximum equilibrium amount of a solute that can be dissolved to a certain amount of solvent under certain conditions, such as temperature and pressure. Solubility constant is used to describe the relationship between the dissolved and solid states of compounds at saturation. Dissolution rate, on the other hand, describes the kinetics of the dissolution and is dependent also on some other factors, such as the particle size of the solid material (particulates).

The dissolution of magnetite at the oxide-water interface involves the reduction of Fe(III) to Fe(II) and therefore its solubility is a function of partial pressure of the hydrogen in the system [10]. Fe_3O_4 solubility has been measured under varying hydrogen pressures and temperatures in several studies [10, 11]. Experimentally measured solubilities of magnetite at different pH and temperatures are shown Fig. 2.

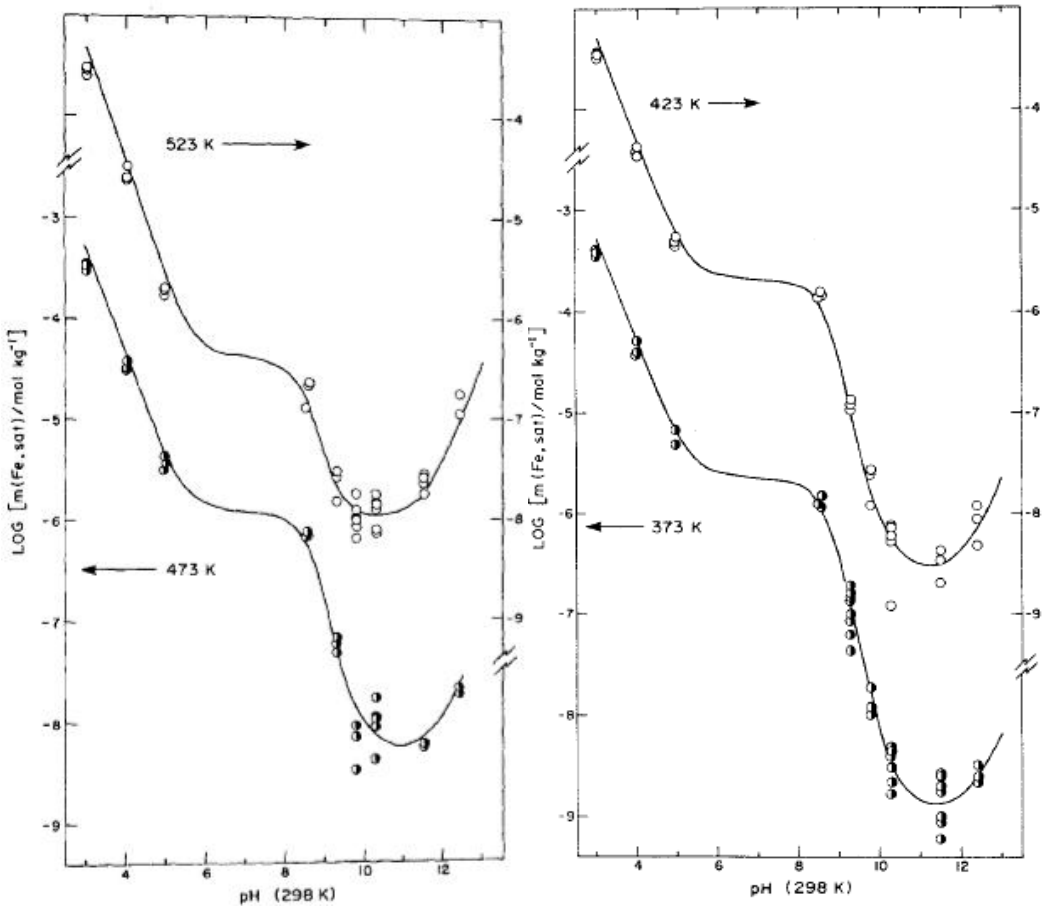

Figure 2: Solubility of Fe_3O_4 at 523, 473, 423 and 373 °K and 779 mol/kg H_2 [10]

Dissolution of magnetite and formation of dissolved ferrous or ferric species is described by Eqs. 10 and 11.

$$\frac{1}{3}Fe_3O_4 + (2-b)H^+ + \frac{1}{3}H_2 \leftrightarrow Fe(OH)_b^{(2-b)} + (\frac{4}{3}-b)H_2O \qquad (10)$$

$$\frac{1}{3}Fe_3O_4 + (3-b)H^+ \leftrightarrow Fe(OH)_b^{(3-b)} + \frac{1}{6}H_2 + (\frac{4}{3}-b)H_2O \qquad (11)$$

Here $Fe(OH)_b^{2-b}$ and $Fe(OH)_b^{3-b}$ are the hydrolyzed species of ferrous and ferric iron. The equilibrium of the aqueous species is described by Eq. 12.

$$Fe(OH)_b^{(2-b)} + H_2O \leftrightarrow Fe(OH)_{b+1}^{3-(b+1)} + \frac{1}{2}H_2 \qquad (12)$$

Polynuclear hydrolyzed species are unstable at the high temperatures and low ionic strengths. The proportion of Fe in the ferric state is negligible at the values of pH less than 9 [11]. Tremaine et al. measured the oxidation state of iron compounds at pH 9.3 (298 °K) and temperature of 373 °K with different H_2 molalities [10]. At H_2 concentration of 779 µmol/kg and pH 9.3 (298 °K) significant proportion of Fe was in ferric form according to the experimental data and thermodynamic calculations. Higher temperature and pH increased the

proportion of the ferric iron. On the other hand, higher H_2 concentration increased the proportion of the ferrous iron.

Molality of the hydrolyzed species in the solution (as per Eqs. 10 and 11) is defined by the solubility constants according to Eq. 13.

$$m(Fe(OH)_b^{Z-b}) = K_{s,b}^{Z}\left[m(H^+)\gamma_1\right]^{Z-b} P(H_2)^{(4/3-z/2)}/\gamma_{Z-b} \quad (13)$$

In Eq. 13 Z = 2 for Fe(II) species and Z = 3 for Fe(III) species. The term $m(H^+)$ is the molality of H^+ in equilibrium saturated solution. The γ are the molal ionic activity coefficients which can be calculated according to extended Debye-Hückels equation. Tremaine et al. used Eq. 14 to describe the temperature dependence of the solubility constants [10]:

$$\begin{aligned} -RT\ln K_{s,b}^{Z} &= \Delta G_R^{\circ}(Fe(Fe(OH)_b^{Z-b}, T) \\ &\approx \Delta G_R^{\circ}(Fe(Fe(OH)_b^{Z-b}, 298^{\circ}K) - \Delta S_R^{\circ}(Fe(OH)_b^{Z-b})\left[T - 298\right] \end{aligned} \quad (14)$$

Major ferrous and ferric species formed from the magnetite at normal NPP pH range at 423 °K are Fe^{2+} and $Fe(OH)_2$ whereas at 573 °K they are Fe^{2+}, $Fe(OH)_2$ and $Fe(OH)_3$ [10]. $Fe(OH)^+$ is a minor species that contributes to no more than 20% at any pH. Proportion of $Fe(OH)_4^-$ and $Fe(OH)_3^-$ increases significantly at high pH (> 10). The solubility and hydrolysis constants for the formation of Fe^{2+} (Eq. 15), $Fe(OH)_3$ and $Fe(OH)_4^-$ (Eq. 16) from Fe_3O_4 and hydrolysis constants for the ferrous species $FeOH^+$, $Fe(OH)_2$ and $Fe(OH)_3^-$ (Eq. 17) are shown in Table 2.

$$K_{s,0}^{II} = m(Fe^{2+})\gamma_2 = \left[m(H^+)\gamma_1\right]^2 P(H_2)^{1/3} \quad (15)$$

$$K_{s,b}^{III} = m(Fe(OH)_b^{3-b})\gamma_{3-b} P(H_2)^{1/6}/\left[m(H^+)\gamma_1\right]^{3-b} \quad (16)$$

$$K_{0,b}^{II} = m(Fe(OH)_b^{2-b})\gamma_{2-b}\left[m(H^+)\gamma_1\right]^{b}/\left[m(Fe^{2+})\gamma_2\right] \quad (17)$$

Table 2: Solubility constant of magnetite and hydrolysis constants of ferrous species [10].

Solubility constants of Fe_3O_4			
T (K)	**$\log_{10} K^{II}_{s,0}$ ($kg*mol^{-1}*atm^{-1/3}$)**	**$\log_{10} K^{III}_{s,3}$ ($mol*atm^{1/6}*kg^{-1}$)**	**$\log_{10} K^{III}_{s,4}$ ($mol^2*atm^{1/6}*kg^{-2}$)**
373	8.23	-11.05	-20.00
423	6.94	-10.16	-18.90
473	5.92	-9.45	-17.85
523	5.10	-8.88	-17.08
573	4.42	-8.41	-16.45
Hydrolysis constants of Fe^{2+}			
T (K)	**$-\log_{10} K^{II}_{0,1}$ ($mol*kg^{-1}$)**	**$-\log_{10} K^{II}_{0,2}$ (mol^2*kg^{-2})**	**$\log_{10} K^{II}_{0,3}$ (mol^3*kg^{-3})**
373	8.78	17.15	28.11
423	8.09	15.44	25.63
473	7.56	14.09	23.68
523	7.12	12.99	22.10
573	6.79	12.09	20.80

The solubility of magnetite decreases when temperature increases except in highly alkaline solutions (Fig. 3) [10]. The change of solubility with temperature affects the FAC rate and also the rate of magnetite deposition. At highly alkaline solutions at high temperatures magnetite solubility increases when temperature increases. According to data of Tremaine et al., positive solubility-temperature gradient occurs at pH (298 °K) ≥9,4 at temperature of 573 °K and at pH (298 °K) ≥9,9 at temperature of 423 °K [10].

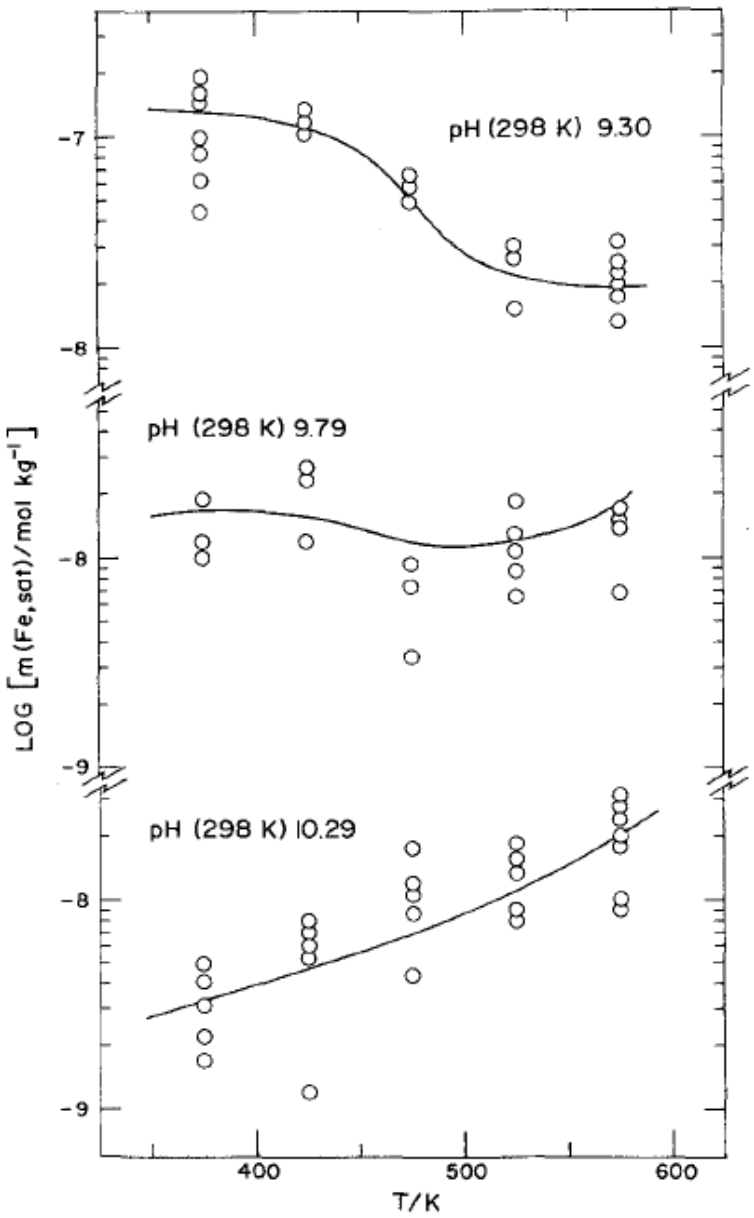

Figure 3: The temperature dependence of magnetite solubility at 779 µmol/kg H_2 and at different pHs [10].

3.1.2 Single- and two-phase FAC

FAC can occur in both single-phase and two-phase flows. Single-phase FAC is defined as flow-accelerated corrosion occurring in water stream, whereas two-phase FAC occurs in a water-steam system. It should also be noted that FAC does not occur in dry steam.

The visual appearance of the steel surface depends on the type of the flow. The surfaces experiencing single-phase FAC often look like "orange-peeled" (Fig. 4) and have small cavities in them [12]. The size of the cavities can vary and can sometimes have a mean diameter of larger than 5 mm. However, the cavity diameter is not directly linked to the degree of degradation. Areas with very high FAC rate can have a polished appearance with no cavities. In certain areas, in which the rate of FAC is slow, pit-like features are encountered on the surface. Regardless of their appearance, all such features have directionality with a tip pointing to the flow direction. When FAC progresses at the surface, these "chevrons" or "horseshoes" overlap and surface starts to look as "orange peeled". The magnetite layer on such surfaces is very thin (less than 1 µm).

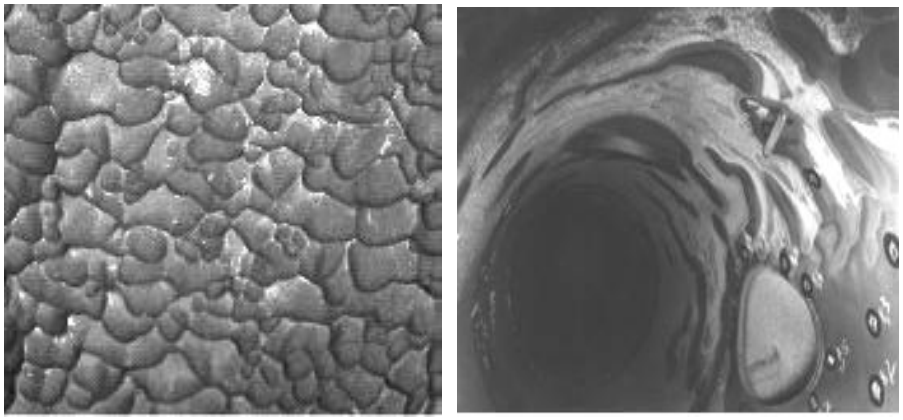

Figure 4: "Orange-peel" surface of the single-phase FAC (on the left) and "tiger-striped" surface of the two-phase FAC (on the right) [12].

Surfaces on which two-phase FAC occurs often have a "tiger-striped" appearance as shown in Fig. 4 and the damaged area is often characterized by a black shiny surface [12]. Two-phase FAC areas with an oxide layer are always black because possible oxygen in the water is removed to the steam phase. According to Dalton's law, the oxygen in a saturated steam-water mixture is mostly located in the steam if the concentration of oxygen is less than 100 µg/l [6]. Two-phase FAC is more aggressive than single-phase FAC due to the hyper-turbulent nature of wet steam when compared to a single phase water stream.

3.1.3 FAC prone areas

FAC has caused incidents in both nuclear and fossil-fuel power plants [13]. Various plant areas with carbon steel can be susceptible. Schematic picture of FAC prone locations is shown in Fig. 5.

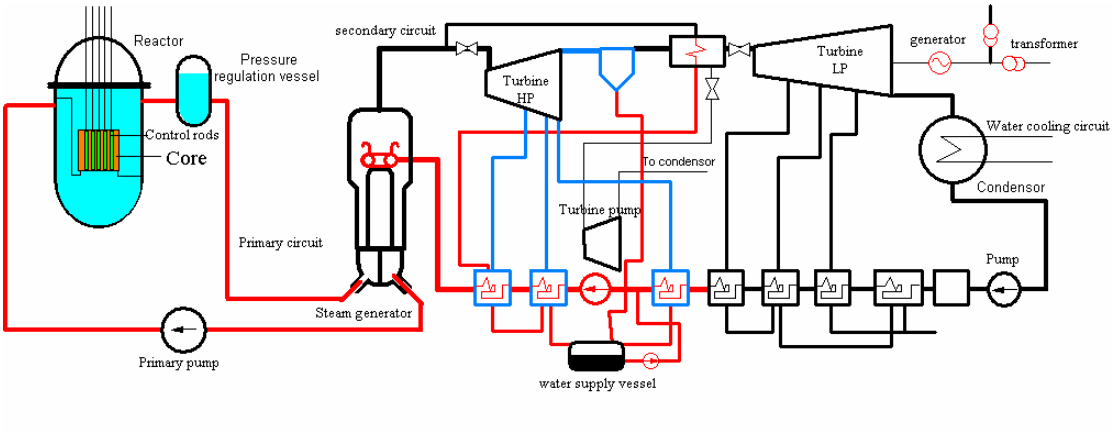

Figure 5: The schematic picture of the potential FAC locations. FAC prone areas are marked with red color [13].

Components that can promote the formation of vortices, secondary flows or turbulence are prone to FAC. These include elbows, bends, tees, reducers, pipe entries and components downstream of valves and flow-control orifices. At NPPs the places that can be affected by single- or two-phase FAC are [14, 15]:

Single-Phase Systems

- Condensate and feedwater systems
- Auxiliary feedwater systems
- Heater drain lines
- Moisture separation drains
- Steam generator blowdown systems
- Reheater drains
- Other drains

Two-Phase Systems

- High- and low-pressure extraction steam lines
- Flashing lines to the condenser (miscellaneous drains)
- Gland-steam (seal-steam) systems
- Feedwater heater vents

Kain et al identified systems that were vulnerable to FAC according to ultrasonic thickness (UT) inspections [16]. They were parts of feed water line downstream of control valves, downstream of control valve of reheater drain, separator drain, bleed steam drain alternate and main path, extraction lines, steam drain system, heater vents downstream of restriction orifices and heater drain system downstream of control valves. They also found out that thickness reduction was noticeable in blow down system, moisture separator and re-heater drain system where bulk velocity was lower than normally recommended. Degradation was noticed at temperatures from 90 °C to 250 °C.

Table 2 lists the most significant FAC incidents until 12/2005. It can be noticed that despite the development made in FAC related areas there has been several

events even in recent years. Steam and water leaks after rupture affect safety and non-safety related equipment and also cause personnel safety concerns.

Table 3: Most significant FAC incidents through 12/2005 (reproduced from [14]).

Plant	Type	Date	Phase	System
Oconee	PWR	6/82	Two-phase	Extraction
Navajo	Fossil	11/82	Single-phase	Feedwater
Surry	PWR	12/86	Single-phase	Condensate
Trojan	PWR	6/87	Single-phase	Feedwater
Arkansas Nuclear One	PWR	4/89	Two-phase	Extraction
Santa Maria de Garona, Spain	BWR	12/89	Single-phase	Feedwater
Loviisa, Finland	PWR	5/90	Single-phase	Feedwater
Millstone 3	PWR	12/90	Single-phase	Separator drain
Millstone 2	PWR	11/91	Single-phase	Reheater drain
Sequoyah	PWR	3/93	Two-phase	Extraction
Sequoyah	PWR	11/94	Single-phase	Condensate
Pleasent Prairie Power Plant	Fossil	2/95	Single-phase	Feedwater
Millstone 2	PWR	8/95	Single-phase	Heater drain
Fort Calhoun	PWR	4/97	Two-phase	Extraction
Point Beach 1	PWR	5/99	Two-phase	Feedwater heater
Callaway	PWR	8/99	Two-phase	Reheater drain
H.A. Wagner 3 Power Plant	Fossil	7/02		Feedwater heater line
Mihama 3, Japan	PWR	8/04	Single-phase	Feedwater
Edwards Power Plant	Fossil	3/05	Single-phase	Feedwater
South Ukraine 2	VVER	7/05		Feedwater heater line
South Ukraine 2	VVER	8/05		Reheater drain

3.2 Parameters influencing rate of flow accelerated corrosion

3.2.1 Oxidizing/reducing agents and electrode potential

Redox-potential or oxidation-reduction potential (ORP) and more generally the corrosion or mixed potential (ECP) is an indicator which gives information about the balance between the reducing and oxidising agents [4, 5]. The major contributors to the ECP values in NPP water systems are dissolved oxygen, hydrazine and dissolved iron. ECP has been recognized as the most important parameter influencing the single-phase FAC. Concerning two-phase FAC conditions, oxygen partitions to the steam-phase and therefore the possible positive effect of oxygen on FAC rate does not apply to such conditions.

In secondary circuit of power plants reducing conditions are considered to occur when water contains less than 10 µg/kg oxygen and a reducing agent is added to the water [17, 18]. With this water chemistry oxidation-reduction potential (ORP) is in the range of reducing conditions (ORP < 0 mV vs. SCE).

3.2.1.1 Effect of hydrazine

Normally oxygen scavengers, such as hydrazine, are used to protect the steam generator tubing material from stress corrosion cracking (SCC) by positioning the

ECP near the hydrogen line (the potential of the reversible hydrogen electrode) [4]. Hydrazine is a reducing chemical which reacts with oxygen and forms water and nitrogen (Eq. 18). The reaction between hydrazine and oxygen is complex and is strongly temperature dependent [19]. The reaction can be considered slow at feed temperature ~150 °C and faster at >180 °C. At high temperatures, hydrazine can also decompose to ammonia, nitrogen and hydrogen according to equations 19 and 20.

$$N_2H_4 + O_2 \rightarrow N_2 + H_2O \quad (18)$$

$$3N_2H_4 \rightarrow N_2 + 4NH_3 \quad (19)$$

$$2N_2H_4 \rightarrow N_2 + 2NH_3 + H_2 \quad (20)$$

Hydrazine may also react with higher-valency metal oxides by reducing them and forming e.g. magnetite (Eq. 21) and cuprous oxide (Eq. 22).

$$N_2H_4 + 6Fe_2O_3 \rightarrow 4Fe_3O_4 + H_2O + N_2 \quad (21)$$

$$N_2H_4 + 4CuO \rightarrow 2Cu_2O + 2H_2O + N_2 \quad (22)$$

Hydrazine is added to the feedwater of the PWR secondary loops. It maintains reducing environment in the feedtrain and steam generator [4]. When, at higher temperature it decomposes to ammonia it also works as a pH conditioning chemical. It is also necessity in the plants with mixed-metallurgy systems to protect the copper-containing components (e.g. heat exchanger tubing) from dissolving. EPRI guideline recommends feedwater hydrazine to condensate oxygen ratio of at least 8 for adequate control of transport of oxygen and other oxidants to the steam generators [20]. High hydrazine concentration also reduces the problems caused by the stress corrosion cracking of the Alloy 600 tubes. Most of the PWRs in the 1980's and early 1990's ran with low or medium hydrazine concentrations in the feedtrain (about 20 µg/l). During the early and mid 1990's trend was towards higher hydrazine concentrations (>100 µg/l feedwater hydrazine).

However, the decrease in the ECP can lead to faster dissolution during FAC due to the increased reductive dissolution rate of magnetite [4, 5, 21]. Accordingly, FAC rate increases with the dose in the range of 0-150 µg/l. Above 150 µg/l concentration ECP is lowered to level at which the kinetics of dissolution are slower and the FAC rate decreases. However, EPRI has performed a study to examine the role of hydrazine in steam generators and concluded that while hydrazine may have been associated with a few cases of damage there are units with similar designs and water chemistry with high hydrazine levels with no problems and therefore the high hydrazine level is not the most important factor [21].

As stated above, high hydrazine concentrations (>150 µg/l) can also have a beneficial effect on FAC rate [3, 21]. Hydrazine increases the pH and may also lead to slower kinetics of dissolution. Experimental results suggest that FAC rate is proportional to hydrazine concentration at the power of 1/6. Eq. 20 has been proposed for dependence of FAC rate at hydrazine concentrations above 60 µg/l:

$$\text{FAC rate} \approx 0{,}925 * [N_2H_4]^{1/6} \quad (20)$$

In the normal hydrazine range (from 50 µg/l to 100 µg/l), FAC rate increases by a maximum factor of 2 as a function of hydrazine concentration (Fig. 6) [22].

According to tests made by EdF, hydrazine concentration has an effect on FAC rate at 235°C but not at 180°C, and the maximum effect found was factor 2 increase in FAC rate [4]. Further studies at 210 °C showed an intermediate result, namely a slight dependence of FAC on the hydrazine concentration [21]. There is still controversy if the hydrazine dependence on FAC is a bell-shaped curve with a maximum at about 150 µg/l, or, alternatively, FAC rate increases monotonically with hydrazine concentration. High hydrazine concentration may change the character of the iron oxide which could explain the bell-shaped curve. However, recent tests designed to confirm the results at 235 °C with less scattered data have been unsuccessful [23]. An additional result from these tests was the long-term effect of hydrazine when concentration was reduced from a high value to zero. This could be related to effect of hydrazine on oxide porosity.

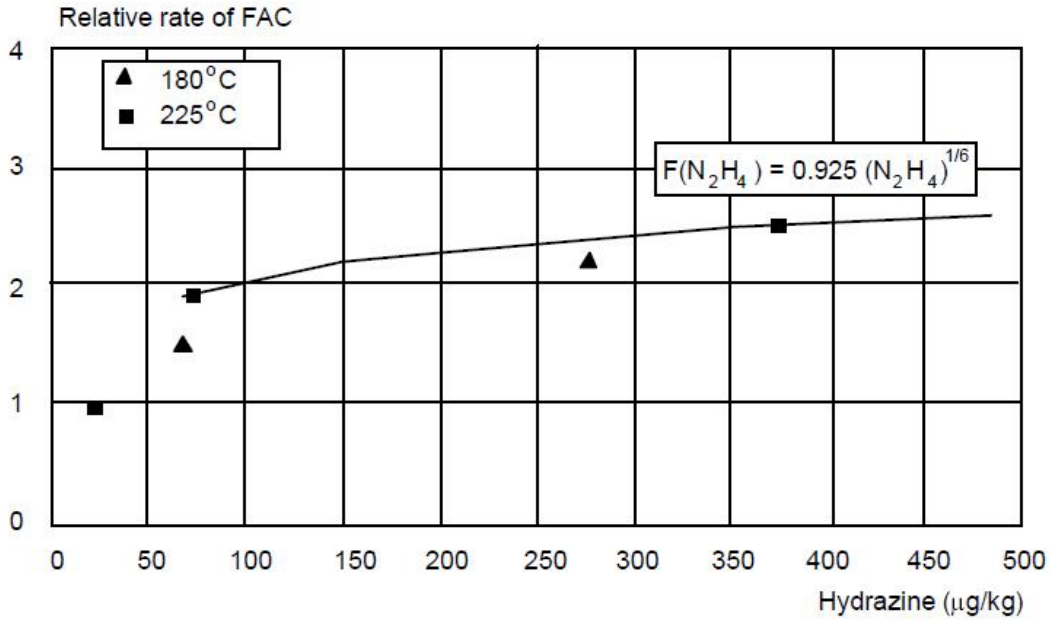

Figure 6: Effect of hydrazine concentration on FAC rate [22].

According to plant data a high concentration of hydrazine does not have a significant effect on ECP [4]. It seems that hydrazine concentration has a threshold value above which the electrochemical potential of construction materials is nearly independent of the hydrazine concentration. ECP was monitored at Comanche Peak and good correlation between ECP and feedwater oxygen was found. However, there was no significant correlation between ECP and hydrazine concentration when concentration was from 30 µg/l to 700 µg/l.

According to the results at South Texas Project unit 1, changing the injection point of hydrazine from the condensate system to after HP heater did not have significant effect on ECP or corrosion product transport (CTP) [4]. It seemed that the low dissolved oxygen concentration (< 1 µg/l) controlled the FAC rate and therefore the injection location did not have significant effect. According to these

results, in the normal hydrazine concentration range ECP is controlled by dissolved oxygen level.

Changing the oxygen scavenger from hydrazine to other chemicals, such as hydroxylamine and DEHA, can have an effect on FAC rate [4]. Feedwater iron concentrations were reduced to less than 0.1 µg/l when oxygen concentration was 4 µg/l and DEHA was used for oxygen control. According to the literature, DEHA is a less effective oxygen scavenger than hydrazine and ECP values are higher while it is applied. According to the cited results, 30 µg/kg of hydrazine is more efficient in decreasing the oxygen concentration in the feedwater than 50 µg/kg of DEHA [24]. Similar results have been obtained with hydroxylamine in the boiler at a pulp and paper mill. Feedwater iron was reduced to less than 1 µg/l within a month when hydroxylamine was used and returned to 4-6 µg/l when hydrazine was reapplied.

3.2.1.2 Effect of oxygen

While nuclear industry commonly uses increased hydrazine concentration, a large share of fossil plants has eliminated the use of hydrazine [3, 5]. In the fossil and industrial plants oxidizing environment (with ORP > 0 mV vs. NHE) can be utilized with all-ferrous feedwater systems (AVT(O) and OT). In AVT(0) treatment type all-volatile treatment is used without reducing agent whereas in OT treatment oxygen is added to water. In OT treatment, surface is covered with a layer of ferric oxide hydrate (FeOOH) or hematite (Fe_2O_3) which also goes inside the pores of the magnetite (Fig. 7). Ferric oxide layer functions as a boundary barrier for the inward diffusion of oxygen to the base material and Fe^{2+} ion transport from the steel surface through the magnetite layer. The presence of FeOOH and Fe_2O_3 also reduces the overall solubility of the oxide layer, because FeOOH and Fe_2O_3 have lower solubility than Fe_3O_4. The rate of conversion of Fe_3O_4 to FeOOH or Fe_2O_3 depends on the degree of oxidizing conditions.

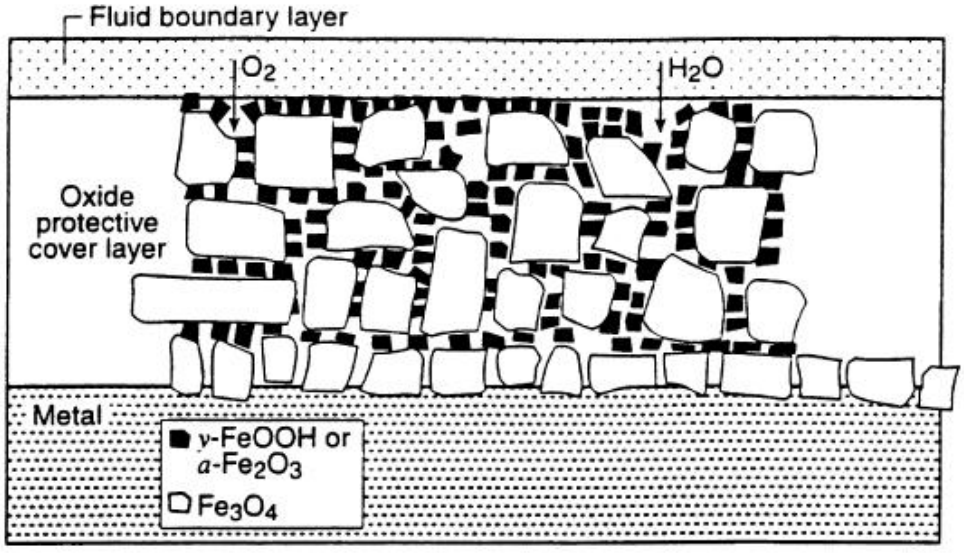

Figure 7: Surface oxides formed on carbon steel surfaces with oxidizing feedwater chemistry (ORP > 0mv) [3].

In the presence of oxygen magnetite is in equilibrium with hematite according to Eq. 23. According to thermodynamical calculations at 423 °K, oxygen is consumed and hematite is formed eventually when oxygen concentration is higher than $4{,}97*10^{-48}$ mol/kg.

$$2Fe_3O_4 + \frac{1}{2}O_2 \leftrightarrow 2Fe_2O_3 \qquad (23)$$

Equilibrium of Fe_3O_4 with ferrous iron was presented in Eq. 12. H_2 concentration required to hold this equilibrium is dependent on pH [25]. According to equilibrium concentrations of oxygen and hydrogen, magnetite system is much more sensitive to the presence of oxygen than to the presence of hydrogen.

There is a decrease of more than four orders of magnitude in the FAC rate of low-alloy steel in water at 120 °C when oxygen concentration is 150-500 µg/l when compared to deoxygenated conditions [4]. More importantly, considerably smaller oxygen concentrations, such as 10 µg/l, can reduce FAC even when large excess of hydrazine is present in the water [21, 26]. This has been demonstrated both in the PWR and fossil plants. Oxidizing conditions will exist in the systems with reducing agents when oxygen level is only slightly above 10 µg/l, whereas at oxygen concentration of 30-150 µg/l the electrochemical potential of the steel increases with hundreds of millivolts resulting in other corrosion problems [5, 27]. According to investigations in the test loops and plant data, the lowest threshold limit for the reduction of FAC with oxygen is 1 µg/l. The low-oxygen water chemistry has been demonstrated at Millstone 2, where condensate oxygen concentration was allowed to increase to about 10 µg/l [21]. Controlled air-leakage injection decreased the iron transport to the steam generators by 40%. British Energy used oxygen dosing for more than 20 years to control FAC in their AGR boilers [26]. They used 15-25 µg/kg oxygen concentration to control FAC and simultaneously used hydrazine to avoid SCC risk in the upper part of the boiler.

Research work made by CEGB in 1980's examined the effect of oxygen on FAC damage under boiler feedwater conditions using orifice assembly specimens [26]. They measured in-situ corrosion rate using ^{56}Co activated specimens and ECP of the specimen using Ag/AgCl reference electrode with a junction close to the region of the maximum damage. Experiments were done using temperatures from 115 °C to 210 °C and pH (25 °C) from 7.0 to 9.4. FAC rates were up to 2.2 mm/a under deoxygenated feedwater conditions. They found out that even high FAC rate can be completely suppressed by using low levels of oxygen. Oxygen was also effective in the presence of excess hydrazine and suppression of FAC rate was accompanied with a relatively small shift in ECP (Fig. 8). Results were similar throughout the tested temperature range. The FAC rate, under these conditions, was claimed to be related to the mass transfer of oxygen according to Eq. 24.

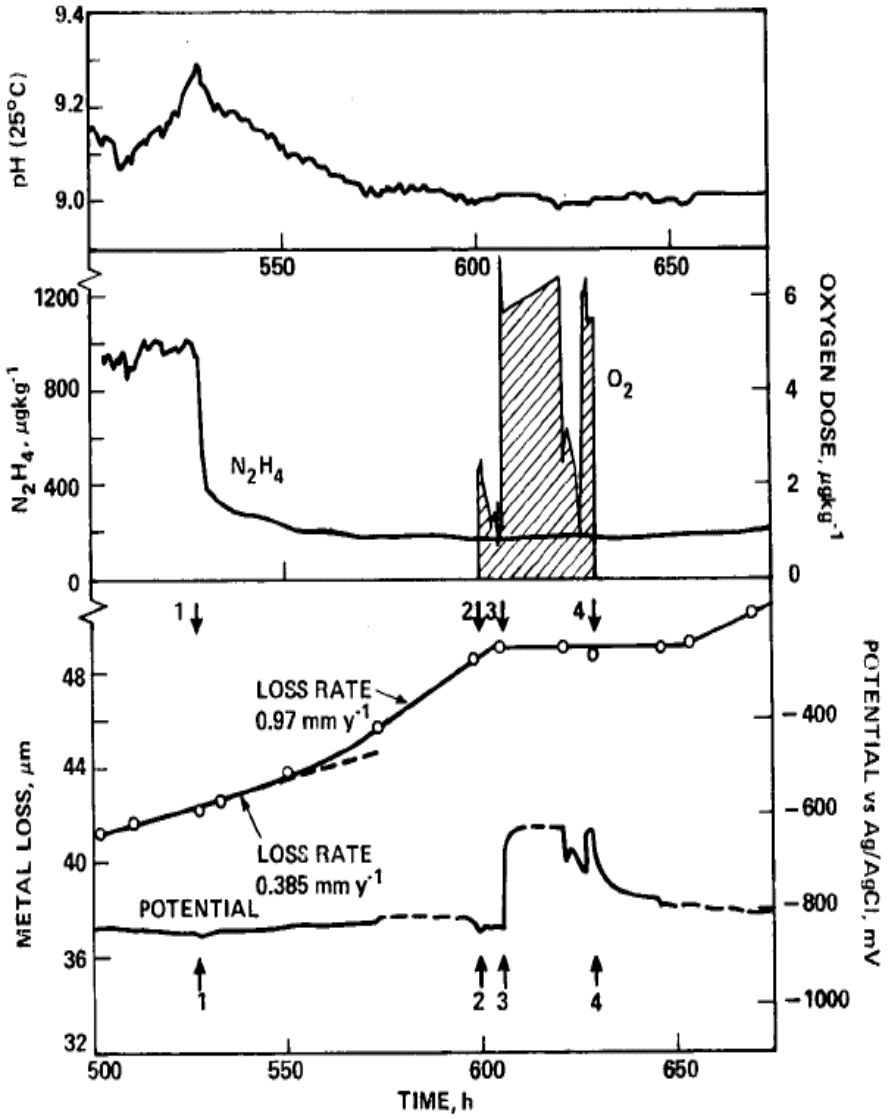

Figure 8: The effect of oxygen dose to FAC rate in test system (180 °C) [26].

$$V_{TC} = K_{O_2} C_{O_2} \rho_w \qquad (24)$$

Here ρ_w is the density of water and k_{O2} and C_{O2} are mass transfer of oxygen to surface and feedwater oxygen concentration. According to results of CEGB, mass transfer of oxygen controls the concentration needed to suppress the FAC [26]. Higher oxygen concentration is needed when mass transfer of ferrous species is fast from the surface to bulk water, such as conditions with low pH and low Cr content, or when mass transfer rate of oxygen to the surface is low.

While there are laboratory results which show that FAC rate is effectively reduced at dissolved oxygen levels greater than about 1 µg/l, plant experience shows considerable FAC at comparable conditions in the feedwater [21]. This can be related to differences in mass transfer behavior of oxygen from the bulk fluid to the corroding wall in laboratory and plant environments. Another report states that many feedwater oxygen measurements have been shown to be incorrect and there has been substantially more oxygen in the bulk water than previously measured.

Higher oxygen concentrations were measured when local monitoring equipment was installed. Especially long sampling lines can cause inaccuracy in oxygen monitoring as shown in Fig. 9.

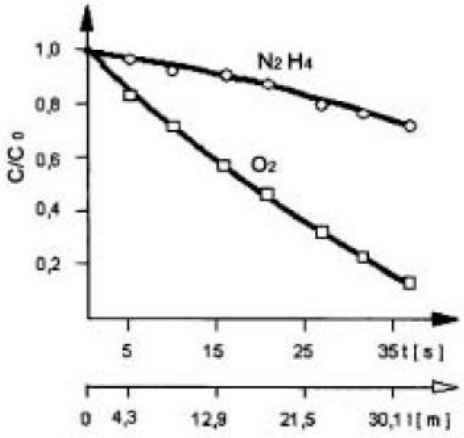

Figure 9: Laboratory data showing the change in concentration of oxygen and hydrazine as a function of duration time (flow rate 35 l/h) and length of a preconditioned stainless steel sampling line of 4 mm internal diameter at 170 °C and 80 bar. Inlet concentrations: O2 = 20 µg/l, N2H4 = 150 µg/l, NH3 = 1 ppm; tube preconditioned with oxygenated water.

3.2.2 Temperature

Rate of FAC is temperature dependant and maximum rate of single-phase FAC occurs at temperatures of 150 ± 20°C [3, 4, 29]. However, FAC occurs in the temperature range of 75-300°C and serious incidents of FAC have occurred across the temperature range of 142-232°C. According to BRT-CICERO software, FAC rate changes as a function of temperature as shown in Figs. 10 and 11.

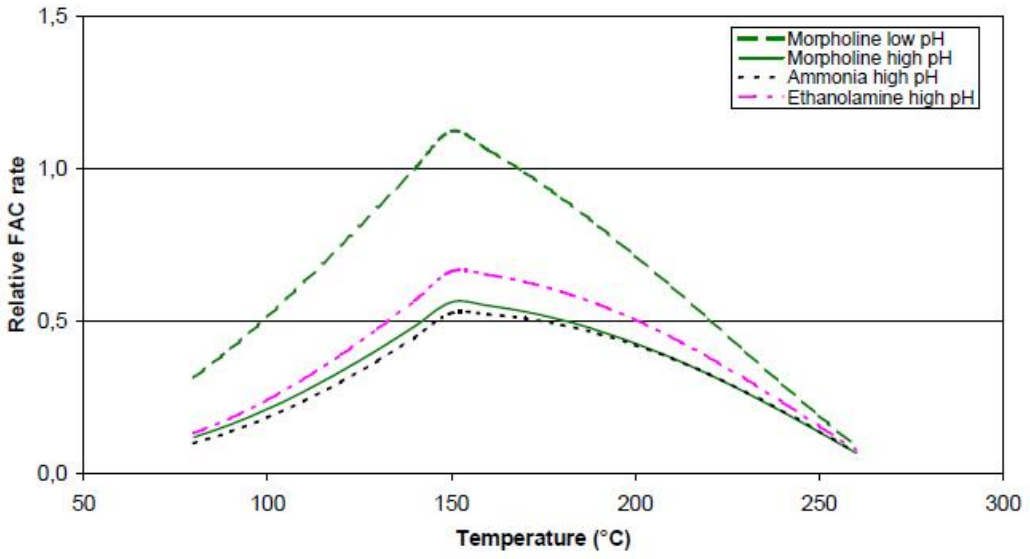

Figure 10: Relative FAC rate calculated with BRT-CICERO™ for 4 types of conditioning under one-phase flow conditions [29].

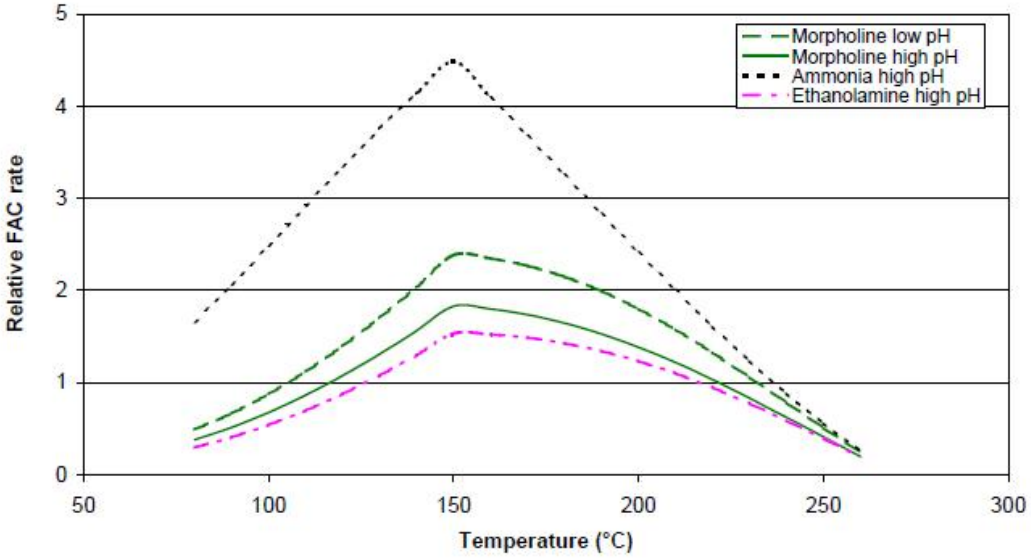

Figure 11: Relative FAC rate calculated with BRT-CICERO™ for 4 types of conditioning under two-phase flow conditions (steam quality 0.75) [29].

The effect of temperature is related to two phenomena [6]. When temperature increases the magnetite solubility decreases. However, temperature also affects the flow viscosity and diffusion coefficient of ferrous ions. This means that C_{eq} is highest at low temperatures and K_m is highest at high temperatures. From eq. (9) it is obvious that a maximum in V_{TC} as a function of temperature such as that shown in Figs. 10 and 11 should occur. However, FAC rate can be high at low temperature when flow conditions correspond to high mass transfer. On the other hand, when water chemistry causes low dependence between soluble ferrous ion concentration and temperature FAC rate can be high at high temperatures. The temperature of the maximum FAC rate increases with increasing mass transfer.

Recently there have been several reports of FAC damages at low temperatures [30, 31]. Low temperature in this case can be defined to be less than 90 °C. Crockett et al. have presented five cases where low temperature FAC-like damage has occurred at NPPs [30]. Cases were immediately downstream of the condensate polishers or downstream of the steam generator blowdown demineralizers. Surface morphology of damaged surfaces was very similar to conventional, single-phase FAC. For PWRs, the authors recommend susceptibility evaluations and inspections in the resin traps and in the areas of piping between the discharge of the polishers and the amine injection point and also downstream of the steam generator blowdown demineralizers. They also suggest the relocation of amine injection point further upstream to reduce vulnerability to low temperature attack. For BWR evaluation, all low-oxygen areas of the condensate, feedwater and auxiliary systems should be ensured. They conclude that it is poor water chemistry rather than low temperature that causes high wear rates at low temperatures.

3.2.3 pH

The at-temperature pH has first-order effect on FAC rate due to its effect on magnetite solubility [5, 10]. The potential-pH diagram of the Fe-water system at 150 °C is presented in Fig. 12. As stated in chapter 3.1., magnetite dissolution involves a reduction reaction and is therefore dependent on E-pH conditions. Small changes in at-temperature pH can have major influence on solubility of magnetite and consequently on the FAC rate. According to literature, solubility of magnetite at 198 °C decreases by a factor of 2 for every 1 unit of at-temperature pH above pH 5.3 [4].

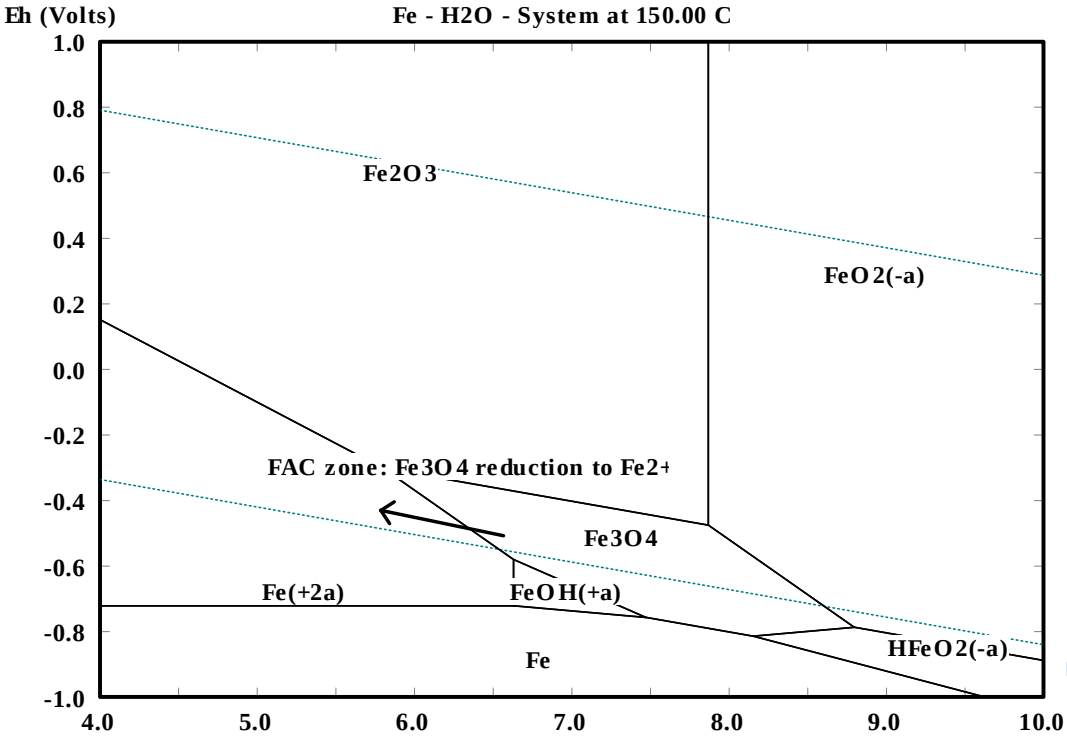

Figure 12: The potential-pH diagram at 150 °C and area of FAC, where Fe_3O_4 reduction to Fe^{2+} occurs (at-temperature pH).

According to Watanabe et al., FAC rate has a nonlinear dependency on pH [32]. Removal rate was found to decrease steeply around pH 9.0 to 9.5 (Fig. 13). FAC rate followed the form of the magnetite solubility curve. However, while solubility decreases by two orders when pH changes from neutral to 10.4, FAC rate decreased only by one order of magnitude. Eqs. 8 and 9 assume a linear dependency of FAC rate on magnetite solubility, which may be an overestimation according to results of Watanabe et al.

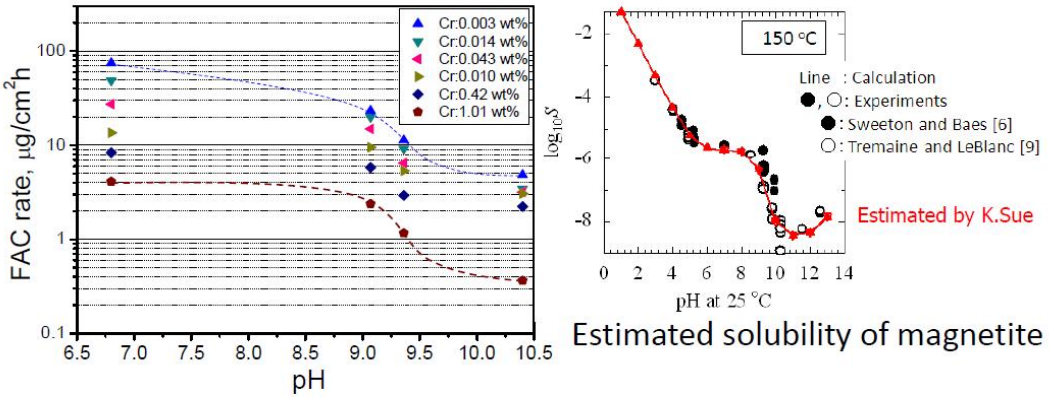

Figure 13: FAC rate as function of pH according to Watanabe et al. [32] and estimated solubility of magnetite according to Sweeton et al. [11] and Tremaine et al. [10]

The effect of different pH adjusting chemicals on the FAC rate is unclear. There are studies in which researchers concluded that only at-temperature pH is a significant parameter [29]. However, there are also studies, the results of which are not supporting this conclusion and show that chemical compound by itself may have an effect on the FAC rate [33, 34].

According to results obtained with mixed amine chemistry (ETA, DMA and ammonia) at 225 °C, FAC rates were higher with mixed chemistry compared to ammonia-only chemistry despite the elevated pH of the mixed amines [34]. The choice of amine may have a second order effect on corrosion rate. Further, amine specific effect was lessened by chromium additions to the steel. The effect was also identified at higher temperatures (282 °C). At this temperature, FAC rates were consistently higher in a mixed amine solution than in ammonia even when at-temperature pH was the same [33]. According to Fukumura et al., the peak FAC rate shifts to higher temperature after ETA injection [35]. At high temperatures the mass transport though the fluid boundary layer is believed to be the rate determining process and FAC rate becomes controlled by the solubility of iron [4]. There is further evidence of amine-specific effect where amines affect the solubility of the iron possibly as weak complexing agents.

Nasrazadani et al. studied the effect of amines on the oxide particle size and morphology, as well as the relative delay of magnetite to hematite transformation on the steel surfaces exposed to steam [36]. Dimethylamine (DMA) produced needle-like acicular particles of goethite/hematite. 1,8-diazabicyclo[5.4.0]undec-7-ene (DBU) resulted in the formation of more equiaxed particles of magnetite/maghemite. Morpholine addition promoted the agglomeration of thin sharp platelets into coarse flakes of hematite. Particle morphology may also have an influence on deposition and fouling rates.

3.2.4 Material composition

Alloying elements have significant effect on FAC rate. Especially the addition of Cu and Cr has been shown to decrease FAC rate [37]. These elements change the

nature of the oxide layer. The E-pH diagram of the Fe-Cr-water system at 150 °C is presented in Fig. 13. When this diagram is compared to that shown in Fig. 12 it can be concluded that the formation of $FeCr_2O_4$ is thermodynamically favored in wide pH and potential area and also in the area where FAC occurs with unalloyed iron.

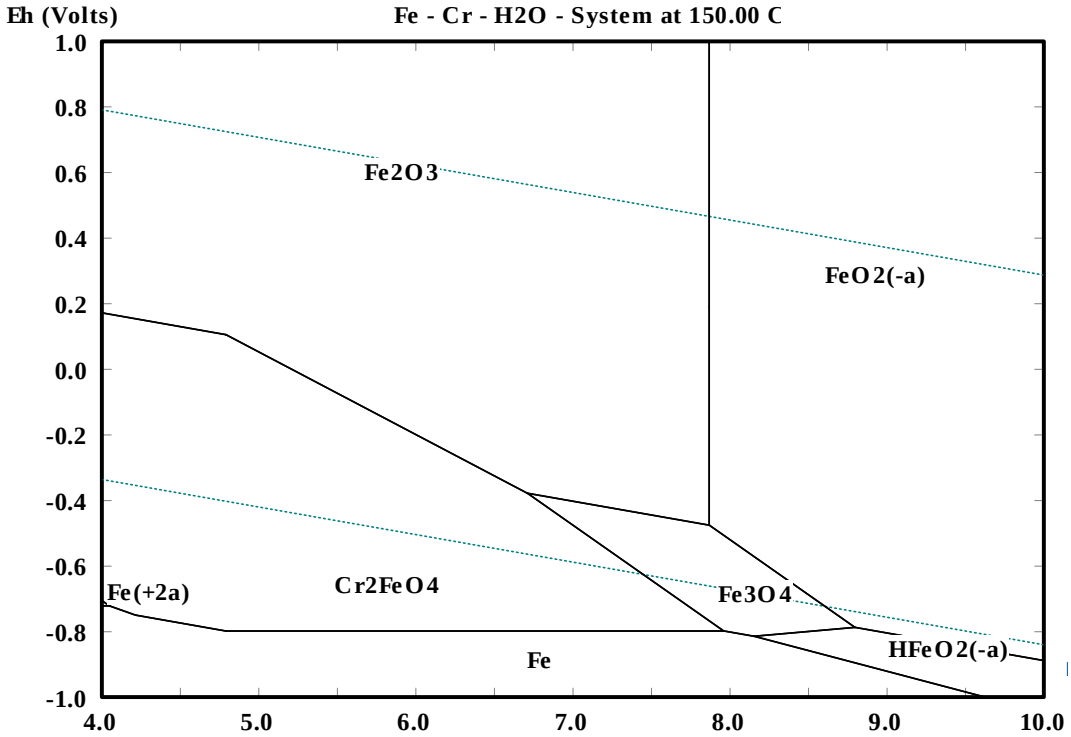

Figure 14: The potential-pH diagram of Fe-Cr-system at 150 °C. Concentrations of dissolved species are 10^{-6} mol/kg.

When Cr is present in the alloy, the equilibrium composition of surface oxide is $FeCr_2O_4$ and the solubility of iron is controlled by Eq. 25 [37].

$$Cr_2FeO_4 + H^+ \leftrightarrow FeOH^+ + Cr_2O_3 \qquad (25)$$

The solubility of $FeCr_2O_4$ is approximately 1/1000 of the solubility of pure magnetite at the same conditions. Consequently, the FAC rate is reduced due to the lower solubility of the oxide layer [37].

$$Cr_2O_3 + 2e^- + 6H^+ \leftrightarrow 2Cr^{2+} + 3H_2O \qquad (26)$$

In low-alloyed steel the ratio of Cr to Fe can be as low as 1/1000 and in the stainless steels it is approximately 1/5 [37]. The corresponding ratio in the $FeCr_2O_4$ is 2/1 so it is obvious that at the beginning the oxide layer contains mostly Fe_3O_4 also for low-alloyed steel. When Fe dissolves from the surface, $FeCr_2O_4$ starts to accumulate on the surface due to its lower solubility. This results in time dependence of FAC for fresh components. Oxide layers on alloyed steels can also involve non-stoichiometric spinels ($Fe_xCr_yO_4$).

Effect of alloying metals has been studied by Ducreux and he proposed Eq. 27 as relationship between FAC rate and steel composition [39].

$$\frac{\text{FAC rate}}{\text{Reference FAC rate}} = \frac{1}{83[\text{Cr}]^{0,89}[\text{Cu}]^{0,25}[\text{Mo}]^{0,20}} \quad (27)$$

In Eq. 27 the reference FAC rate was measured on A42 carbon steel containing 0,04% Cr, less than 0,01% Mo and 0,13 % Cu.

Effect of Cr on FAC rate is considered to be time-dependent [15]. According to theoretical model of Bouchacourt, FAC rate is predicted to decrease with Cr, the decrease becoming more pronounced over time (Fig. 15). This is supposedly due to:

- Progressive oxide porosity decreases over time as chromium concentration increases.
- Reduction of oxide solubility as the oxide is enriched with chromium.
- Increase of oxide thickness over time.

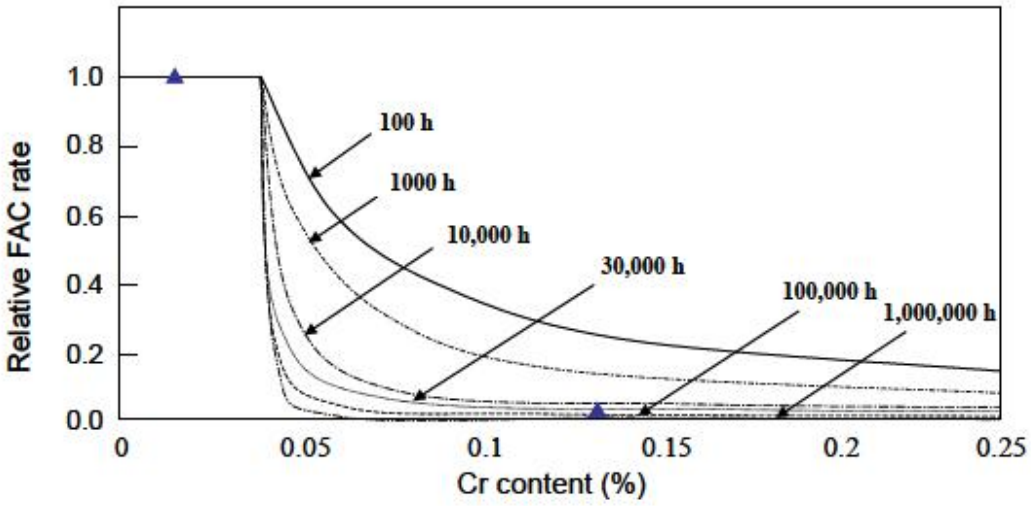

Figure 15: Bouchacourt model where effect of chromium content and time dependency of FAC rate are described [15].

Evolution of FAC rate with time has been studied at EDF's CIROCO loop [38]. Time-dependency of FAC rate, described by Bouchacourt model, was not observed for periods lasting up to 1059 hours. Longer tests might be needed to study transient evolution of FAC rate.

The addition of Cr has a beneficial effect under single- and two-phase conditions [5]. According to Bouchacourt et al., the FAC rate is independent of chromium concentration at the range <0.025% Cr [4]. At higher concentrations than 0,025%, Cr has a significant influence on FAC rate. According to incidents at the heat-recovery steam generators (HSRG), small Cr concentrations of 0.1% have mitigated FAC-problems in the real-world situations. It seems that even small changes in the alloy content can have a significant effect on FAC rate [38].

Combined effects of Cr content and environmental factors, such as pH and dissolved oxygen concentration, on FAC rate are still unclear. Watanabe et al. studied Cr effect at different pHs and flow conditions [32]. According to their results, 1% Cr in the carbon steel can suppress FAC rate by one order of magnitude regardless of the pH, ranging from neutral to slightly basic. When Cr concentration is in the range of 0.03-1% and pH is neutral, FAC rate decreases when Cr concentration increases. Under higher pH, there is a threshold Cr concentration around 0.5% after which FAC rate decreases significantly with higher Cr content.

Copper and molybdenum can also reduce FAC rate [37]. Mechanism of FAC rate reduction with copper addition is not analogous to that for Cr, because no stable Fe-Cu-oxide is formed in NPP water environment. Stable compounds formed are Fe_3O_4 and Cu-metal. When iron is oxidized to Fe_3O_4 and dissolved into the flowing water, metallic Cu builds up on the surface of the metal. Cu then works as a mechanical barrier that impedes the passage of iron ions to the corrosion film.

3.2.5 Hydrodynamical factors

Hydrodynamical factors, such as flow velocity, geometry and roughness of surfaces, have an influence on FAC rate [1, 6, 4, 5]. FAC seldom occurs in straight pipes but is often encountered in places with hydrodynamic disturbance, such as elbows, tight bends, tees or downstream of valves or control orifices. FAC rate depends on initial condition of the surface. If surface oxide is present on the metal, a long initiation period occurs during which FAC rate is not linear with time. Longer exposure of oxidized surface to FAC conditions leads to linear corrosion rate with time. This happens also when fresh metallic surface is exposed to FAC conditions. Duration of delay period increases when pH increases.

The main hydrodynamic parameters that affect FAC rate are [1]:

1. The fluid velocity (V)
2. The Reynolds number (Re) that is defined in Eq. 28.

$$\mathrm{Re} = \frac{\mathrm{Vd}}{\gamma} \tag{28}$$

   where d is the characteristic dimension (e.g. the diameter for a tube) and γ is the kinematic viscosity.
3. The surface shear stress (τ) that originates from the velocity difference between the metal surface and the fluid. For tubes the surface shear stress can be obtained from pressure drop measurements or calculated according to Eq. 29.

$$\tau = \frac{\Delta \mathrm{P}}{4(\mathrm{x/d})} = \frac{\mathrm{F}\rho \mathrm{V}^2}{2} \tag{29}$$

where ρ is the fluid density, x is the distance along the tube and F is the fanning friction factor, which is a function of Re and tube roughness relative to its diameter.

4. The mass transfer coefficient (K_m) is the parameter that relates the rate (J) of a transport controlled reaction to the concentration difference (driving force), and it includes both diffusional and convectional transport processes (Eq. 30).

$$J = K_m \Delta C \tag{30}$$

The mass transfer coefficient is obtained from the non-dimensional correlation between Sherwood number, Sh (Eq. 31), and the Reynolds number and Schmidt number, Sc (Eq. 32) according to Eq. 33.

$$Sh = \frac{K_m d}{D_p} \tag{31}$$

$$Sc = \frac{\gamma}{D_p} \tag{32}$$

$$Sh = aRe^x Sc^y = a\,Re^x \left(\frac{\gamma}{D_p}\right)^y = \frac{K_m d}{D_p} \tag{33}$$

where x is 0.5-1, y is typically 0.33, d is tube diameter, D_P is mass diffusivity and $\gamma = \mu/\rho$, i.e. the ratio of viscosity and density. The values of the mass transfer coefficient have been calculated or measured experimentally for several geometries and values can be found in the literature.

The mean fluid velocity is not a good indicator of the FAC risk [1]. FAC rate is only weakly dependent on bulk flow velocity. FAC rate increases only about three times when flow rate increases from 1.5 to 9 m/s. Also no threshold fluid velocity value above which FAC starts to accelerate has been measured or predicted.

There are different views about the usefulness of shear stress in predicting FAC rates [1]. Some have stated that τ indicates the force applied to corrosion products by the fluid, and with sufficient force, corrosion products are removed from the surface. Others have claimed that shear stress is a geometry independent indicator of turbulence in the flow and can thus be used to predict flow accelerated corrosion. However, it is difficult to measure τ locally and it seems that it does not correlate with corrosion rate, mass transfer or turbulence (Fig. 15).

The mass transfer coefficient is the most important parameter when predicting FAC rate [1]. To predict the FAC rate, mass transfer coefficient needs to be measured with sufficient accuracy. The relationship between mass transfer and FAC has been approached by laboratory measurements and by collecting data from operating plants. It seems that the correlation is not always linear. Non-linearity can occur in the following situations:

- Surface film is removed above critical K_m.
- Interactions of anodic and cathodic areas occur.
- Dual control when corrosion rate is partially controlled by activation.

Above a critical Reynolds number, surface roughness develops on the surface [1, 5]. Higher initial roughness and smaller diameter of the tube decreases critical Re. Developed roughness increases mass transfer and corrosion rate. The effect is different depending on geometry. Developed roughness increases upper bound value of Sh by Eq. 34.

$$Sh = 0.01\,ReSc^{0.33} \tag{34}$$

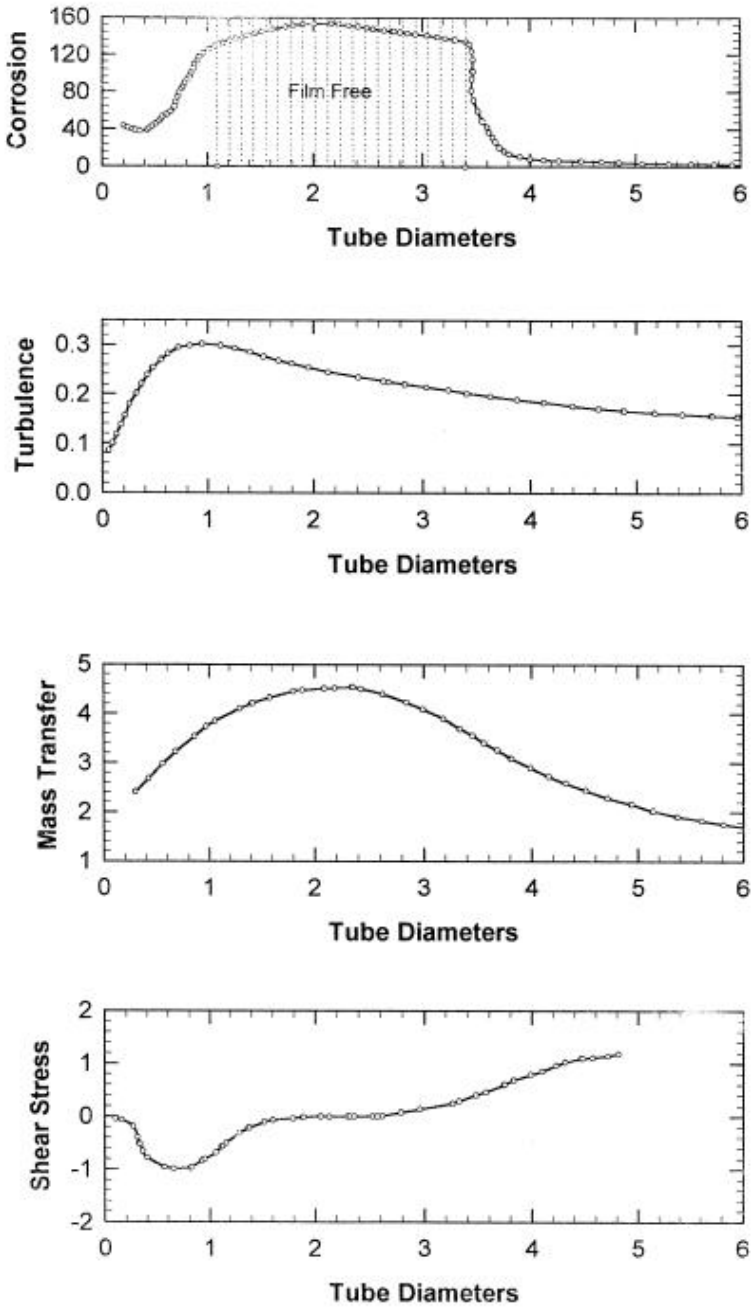

Figure 16: Schematic presentation of variations of corrosion rate, turbulence, mass transfer and shear stress downstream of flow expansion [1].

4 Magnetite deposition

Theories of magnetite deposition fall into two groups:

1. Chemical processes involving crystallization from solutions.
2. Physical processes which depend on adhesion of solid particles to the surface.

The deposition mechanisms are different for soluble species and particulate oxides. Regardless of whether tube scale formation is a chemical or physical process (or both) it occurs in several stages including incubation, initiation (does not apply to particulate fouling), growth, growth limiting stage and spalling and re-deposition. The AECL fouling model includes also a consolidation step, which bonds the magnetite particles chemically and reduces their removal rate from the surface [40, 41].

4.1 Deposition of dissolved iron

Chemical deposition, involving crystallization, can occur in non-boiling, boiling, steaming, or other two-phase environments. Soluble iron is deposited on the surfaces when temperature increases and solubility of the iron decreases (see 3.1.1 Magnetite solubility). It has been suggested that soluble iron can bind magnetite particles (consolidation) and reduce their re-entrainment.

Tomlinson et al. exposed ferritic steel tube to a range of heat fluxes under high temperature and pressure (355 °C, 17.6. MPa, subcooled boiling and bulk boiling to 15% steam quality [42]. According to their results the deposition rate of magnetite from solution increased rapidly with heat flux up to ~900 kW/m^2 and maximum deposition rate was observed at ~1200 kW/m^2. They concluded that rapid increase in deposition rate was associated with the concentration of soluble iron in the microlayer beneath the growing steam bubbles. At higher heat fluxes deposition rate slowed down which could be due to formation of dry patches beneath the steam bubbles.

It has been suggested that magnetite deposition is controlled by the degree of soluble iron supersaturation at the surface according to Eq. 35 [42, 43].

$$V_D = k(C - C_{eq})^n \quad (35)$$

Where V_D is the deposition rate, k is a constant, C is the concentration of soluble iron, C_{eq} is the solubility of magnetite and n is a constant between 1 and 2. Tomlinson et al. suggest that deposition is increased due to:

- Local reduction in magnetite solubility (C_{eq}) when surface temperature increases (as gone through in section 3.1.1 Magnetite solubility). This is important especially at low heat flux.
- Local increase in concentration of soluble iron at bubble nucleation sites. When boiling is occurring on a surface, steam bubbles grow mainly by evaporation from a microlayer of liquid beneath the bubbles. This leads to

high levels of soluble iron in the evaporating microlayer and at the superheated layer/steam interface. This is especially important at high heat fluxes.

Reduced increase of deposition rate at very high heat fluxes occurs when bubble nucleation sites are close to each others and bubble nucleation is fast [42]. Diffusion of soluble iron from the nucleation sites is reduced which increases deposition. However, the formation of dry regions at the evaporating microlayers will reduce the rate of magnetite deposition. As the heat flux increases partial dryout is beginning to affect the magnetite deposition and dryout becomes dominating effect after maximum at 1200 kW/m^2.

Tomlinson et al. suggested that Eq. 36 describes the percentage increase in magnetite deposition due to heat flux [42].

$$\frac{H-I}{I}*100 = 1.0866(e^{(9.4157*10^{-3}Q-3.8084*10^{-6}Q^2)}-1) \quad (36)$$

Where H is the thickness of deposited oxide in heat flux region, I is the thickness of deposited oxide in the non-heat flux inlet region and Q is the heat flux.

It should also be noted that corrosion rate ceases to be controlled by outward diffusion of iron ions through the inner oxide layer when heat flux is greater than ~600 kW/m^2. Instead, according to results of Tomlinson et al., diffusion of water molecules through the outer deposited layer controls the reaction at very high heat fluxes [43].

4.2 Particle deposition models

In the model of Kern and Seaton [44] the net fouling rate of the surface is the difference between the rates of deposition and removal of particles from the heat transfer surface according to Eq. 37.

$$\frac{dm_f}{dt} = \Phi_d - \Phi_r \quad (37)$$

Here m_f is the mass of the deposit in kg/m^2, Φ_d is the particle deposition flux and Φ_r is the particle removal flux in kg/m^{2}s. When linear dependence with the concentration in the bulk liquid is assumed and particles have perfect stickability (all particles adhere to surface), Eq. 38 can be used to describe the deposition flux [45].

$$\Phi_d = K_t(C_b - C_s) = K_d C_b \quad (38)$$

Here K_t is the transport coefficient of the particles, C_b is the concentration of depositing particles in the bulk fluid and C_s is the concentration of adhering particles on the surface. If surface is assumed clean of adhering particles (C_s=0) the transport coefficient becomes identical with the deposition coefficient

(K_t=K_d). Depending of the particle size, either diffusion, inertia or impaction predominate the transport of the particles.

When no perfect stickability is assumed, the deposition stage is generally modeled as a two-step process occurring in series [46]. During the transport step particles are carried from the bulk liquid to the vicinity of the surface. Particles attach on the surface during the attachment step (Eq. 39).

$$\frac{1}{K_d} = \frac{1}{K_t} + \frac{1}{K_a} \tag{39}$$

Where the K_t and K_a are the transport and attachment coefficients.

Lister and Cussac proposed a general equation (Eq. 40) for isothermal, non-boiling and subcooled boiling conditions [47].

$$m(t) = \frac{\Phi_d}{K_r}\left(1 - e^{-K_r t}\right) \tag{40}$$

Here K_r is the removal constant (s^{-1}). The consolidation term is added when the time is greater than critical time, t_c, when consolidation first occurs. The amount of deposited iron oxide under bulk boiling conditions can be calculated by using Eq. 41 [47, 48].

$$m(t) = \frac{\Phi_d}{K_r + K_c}\left[K_c t + \frac{K_r}{K_r + K_c}(1 - e^{-(K_r + K_c)t}\right] \tag{41}$$

where K_c is the consolidation constant (s^{-1}).

4.2.1.1 Isothermal non-boiling transport of particles

Under isothermal non-boiling conditions transport of the particles to the surface can occur by [49]:

- Diffusion transport. The submicron size particles can be treated like large molecules moving with the fluid and not disturbing the flow or turbulence structure. The Brownian motion of the fluid molecules carries them to the wall and transport coefficient, K_t, becomes equivalent to the mass transfer coefficient K_m.
- Inertia. When particle size increases they will have some inertia which is the momentum that is not completely removed in the viscous sublayer. The transition from diffusional to inertial control occurs at particle size of 1-2 µm or greater depending on the conditions, such as viscosity and densities.
- Impaction. When particle size increases sufficiently, particles are less responding to turbulent eddies and their velocity towards the walls approaches friction velocity. In this case particle stopping distance becomes of the same order as the pipe diameter.

Under isothermal and non-boiling conditions for high Schmidt numbers (Sc = $\mu/(\rho D_p)$ ratio of viscous diffusion rate and mass diffusivity), the transport coefficient for diffusion-dominated transport can be calculated according to Eq. 42 [50].

$$K_t = K_{diff} = \frac{0.0840 v^*}{Sc^{2/3}} \quad (42)$$

Here friction velocity v^* is calculated according to Eq. 43.

$$v^* = v\sqrt{f/2} \quad (43)$$

Here v is the bulk flow velocity of the fluid and f is the friction factor obtained from Blasius equation (Eq. 44) for smooth pipe flow.

$$f = \frac{0.791}{Re^{0.25}} \quad (44)$$

When Eq. 42, 43 and 44 are combined Eq. 45 is gained (see also Eq. 31-33) [45, 49].

$$Sh = \frac{K_m d}{D_p} = 0.0167 Re^{0.875} Sc^{1/3} \quad (45)$$

When Stokes-Einstein equation for the Brownian diffusion is used in Eq. 45, the following proportionality is gained:

$$K_t = K_m \propto d_p^{-2/3} v^* \quad (46)$$

Particles are transported by inertia when they are sufficiently large to have velocity that is not completely removed in the viscous sublayer [45, 49]. This momentum can drive magnetite particles to the walls. There is also a phenomenon called turbophoresis which causes migration of particles down the turbulence intensity gradient [51]. Nondimensional transport coefficient, $K_t^+ = K_t/v^*$, against nondimensional particle relaxation time, t_p^+, is used to represent the inertial motion. Particle relaxation time can be described by Eq. 47 and in nondimensional form by Eq. 48.

$$t_p = \frac{s_p}{v_0} = \frac{\rho_p d_p^2}{18\mu} \quad (47)$$

$$t_p^+ = \frac{\rho_p d_p^2}{18\mu} * \frac{(v^*)^2}{v} \quad (48)$$

Transition from diffusional to inertial control occurs at $t_p^+ \approx 0.1$-0.2 which is equivalent to particle size 1-2 µm depending on friction velocity, densities and viscosity. According to Papavergos and Hedley, empirical generalization of

transport coefficient can be calculated according to Eq. 49 for $0.2 < t_p^+ < 20$ (inertia region) [52].

$$K_t^+ \cong 0.00035(t_p^+)^2 \quad (49)$$

Transport coefficient depends on particle size and friction velocity in the inertia region according to Eq. 50[45, 49]:

$$K_t \propto d_p^4 (v^*)^5 \quad (50)$$

When t_p^+ is very high, such as in cases when particle size is sufficiently high or viscosity is low, the particle impaction of particles on the walls will control particle transport and effect of turbulent fluctuations will be limited. When $t_p^+>30$ an approximation presented in Eq. 51 describes the mass transport (impaction region) [52].

$$K_t^+ \cong 0.18 \quad (51)$$

According to Eq. 51, effect of particle size on transport coefficient in this region is nonexistent and following proportionality is gained [45, 49]:

$$K_t \propto (d_p)^0 v^* \quad (52)$$

Other parameters and forces that can have effect on the particle transport in isothermal non-boiling conditions are [45, 49]:

- Surface roughness enhances the transport of particles on the surface by increasing the turbulence level above the roughness elements. Particle deposition can either decrease or increase surface roughness depending on the particle size and initial surface roughness.
- Gravitational force affects when t_p^+ is higher than 1. The gravitational deposition flux can be described by $\varphi_{dg} = v_t C_b$ where C_b is concentration of particles and v_t is terminal settling velocity of particle. For sufficiently large particles gravity controls deposition (sedimentation fouling).
- Lift force can affect particle behavior close to the wall in turbulent flow.
- Viscous interaction force inhibits deposition. It forms when particle approaches the wall and there is an increased viscous resistance, which is caused by the friction between fluid and two approaching surfaces (particle and wall). This force affects especially in liquids.

4.2.1.2 Transport of particles in non-isothermal conditions

Thermophoresis is a force that also affects particles when the particle size is less than 2 µm [53]. Small particles move down a temperature gradient so that cold wall attracts and hot wall repels colloids. Thermophoretic effect increases with temperature gradient but decreases with increasing particle size. Its effect is substantial when heat flux is large. Transport coefficient of thermophoresis can be calculated according to Eq. 53 [54].

$$K_{th} = 0.26 \frac{1}{2\lambda_w + \lambda_p} \frac{\nu_w}{T_{sat}} q \quad (53)$$

Here q is the heat flux, λ_w is the thermal conductivity of water, λ_p is the thermal conductivity of the particle and ν_w is the kinematic viscosity of the water. When thermophoresis is taken into account, the deposition rate coefficient is calculated according to Eq. 54.

$$K_d = K_{diff} - K_{th} \quad (54)$$

4.2.1.3 Effect of boiling on the particle transport

Particulate fouling is more severe under boiling conditions. It has been observed that under boiling conditions, deposits are exclusively formed at the sites of bubble nucleation. The initiation, growth and release of a bubble causes turbulence in the laminary boundary layer adjacent to the tube wall resulting in an influx of water towards the wall to replace the space occupied by the leaving bubble and thereby raising the probability of deposition [47, 55].

Diffusion and thermophoresis have some influence on the deposition also during the boiling especially on the areas with no nucleation sites. Diffusional transport coefficient under boiling conditions can be calculated according to Eq. 55 [47, 53].

$$K_{diff} = (1 - BR) * 0.8 \frac{v^*}{Sc^{3/4}} \quad (55)$$

Where BR is an empirical boiling parameter, which can be calculated according to Eq. 56.

$$BR = \frac{0.05q}{R_b L} \frac{(T_{film} - T_{sat})}{T_{sat}} \quad (56)$$

Here L is the latent heat of vaporization, T_{film} and T_{sat} are the film temperature and saturation temperature (boiling point), respectively. R_b is the bubble radius.

Lister et al. proposed a mechanistic model based on their observation on boiling and of the interactions of nucleating bubbles with suspended particles [47]. They used high speed camera to study the interactions of the bubbles with the particles in a special bubbling tank connected to a recirculating loop. Their model was in good agreement with the experimental data gained by Basset et al [55]. Khumsa-ang et al. confirmed the particulate fouling model experimentally by measuring the deposition of sub-micrometre particles of iron oxides on the Alloy-800 tube [53].

The principle of their model is shown in Fig. 17. It includes the volume of the microlayer (V_1) and the volume of the microlayer evaporated at the centre spot (V_2). Particles are trapped into the skin of the bubble. The number of trapped

particles increases as the bubble grows. Pumping action is caused by the alternation of outflow of liquid during bubble growth followed by the rapid inflow at detachment. Eq. 57 is the expression which describes the deposition at one nucleation site [47].

$$\varphi_{nucl} = \frac{q}{L} K(C_{trapped} + C_{pumped}) \frac{A_{site}}{f} \quad (57)$$

Here f is the bubble frequency, A_{site} is the average surface area of one nucleation site within the radius R_b and K is the dimensionless deposition constant. $C_{trapped}$ is the concentration of particles trapped by the skin of the bubble and C_{pumped} is the concentration of particles in the microlayer caused by the flow through the pumping action.

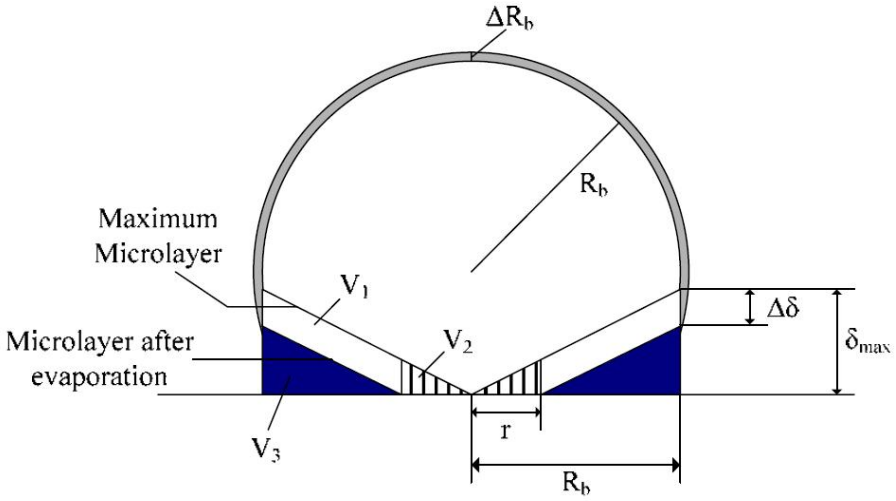

Figure 17: Schematic picture of a nucleating bubble [47].

When particles have attached on the surface the formation of microlayer is disturbed and filtration of particles occurs. Filtration occurs when deposit ring has formed on the nucleation site and liquid, containing particles, passes through this porous layer. Filtration effect is dependent on the amount of deposited material. Filtration flux per one nucleation site for one nucleation can be calculated according to Eq. 58 [47].

$$\varphi_{filt} = C_w \frac{m_{spot}}{8\rho_p} \quad (58)$$

Here C_w is the concentration of particles at the wall and m_{spot} is the mass of iron oxide deposited on the filtration spot. Diffusion also has some effect on deposition rate. The particle concentration on the wall is higher than the concentration in the bulk water. Therefore Eq. 59 is used to describe the diffusion flux (in this case a negative flux) of particles moving away from the nucleation site.

$$\Phi_{diff} = K_{diff}(C_b - C_w) \quad (59)$$

Total particle flux due to boiling at one nucleation site during one nucleation can be calculated according to Eq. 60 [47].

$$\varphi_{boil} = \varphi_{nucl} + \varphi_{filt} + (\Phi_{diff} - \Phi_{th})t_g A_{site} \quad (60)$$

Where t_g is the growth time of one nucleation, A_{site} is the average surface area of one nucleation site and φ_{th} is the flux of particles repelled from the surface due to thermophoresis. During the wait period between bubble detachment and nucleation of next one, only diffusion, thermophoresis and filtration due to pumping effect have an effect on the deposition. This flux (φ_{wait}) on one nucleation site for one waiting period can be calculated using Eq. 61 [47].

$$\varphi_{wait} = (\Phi_{diff} - \Phi_{th})t_w A_{site} + \varphi_{filt} \quad (61)$$

Here t_w is waiting time period between bubble detachment and next nucleation. The total net deposition flux can be calculated using Eq. 62 [47].

$$\Phi_d = N_a f(\varphi_{boil} + \varphi_{wait}) \quad (62)$$

Here N_a is the active nucleation site density and f is the bubble frequency.

Factors in the removal step include dissolution, erosion and spalling. Under flo-boiling conditions, particle removal involves the action of hydrodynamic forces and thermal stresses. Yung et al. have found the re-entrainment of particles to be insignificant when dimensionless average particles size is $0.5 < d_p^+ < 1.3$ ($d_p^+ = d_p v^*/\nu$ where ν is the kinematic viscosity) [56].

Removal of the particles is different in non-boiling, subcooled boiling and bulk boiling conditions [47, 55]. Detaching and collapsing bubbles generate turbulence. Deposit removal is higher in subcooled boiling when bubble collapsing dominates than in bulk boiling during which bubbles detach from surface. During non boiling conditions removal is controlled by diffusion according to Eq. 63.

$$\Phi_r = (C_b - C_s)k_{diff} \quad (63)$$

Under sub-cooled boiling conditions removal is controlled by the collapse of bubbles (Eq. 64).

$$\Phi_r = k_{collapse} C_s \quad (64)$$

The removal constant, $k_{collapse}$, depends on the intensity of the collapsing bubbles, heat flux and latent heat of vaporization (Eq. 65) [47]. Intensity of the collapsing bubbles can be calculated according to Eq. 66.

$$k_{collapse} = \frac{q}{L} I \quad (65)$$

$$I \approx a\rho_w v \frac{R_{bc}^{5/2}}{d_s} \quad (66)$$

Where a is constant, v is the flow velocity in the bulk, R_{bc} is the maximum radius of the bubble before collapsing and d_s is the distance from the surface at which collapse occurs. Intensity of collapsing bubbles decreases when boiling becomes more intense.

Under bulk boiling conditions bubbles are not collapsing or they collapse further away from the surface. In these conditions removal is controlled by the bubble detachment from the surface which causes turbulence at the top portion of the deposit (Eq. 67) [47].

$$\Phi_r = k_{detach} C_s \quad (67)$$

Where removal constant, k_{detach}, depends on the proportion of trapped particles (on the bubble surface) that deposited (ζ=0-1) according to Eq. 68 [47].

$$k_{detach} = \frac{\zeta}{\rho_p} \quad (68)$$

Lister and Cussac [48] have rather successfully applied the above described model to calculate deposition of magnetite both in sub-cooled nucleate boiling and bulk boiling conditions.

There is also phenomena, "heavy fouling under elevated steam quality" (HFESQ), which can be significant for once-through steam generators and very large versions of recirculating steam generators and can lead to heavy fouling in the upper tube bundle [57]. It has been observed that fouling rate by colloidal iron oxides increases dramatically when certain steam quality and mixture velocity are reached. Klimas et al. studied experimentally this phenomenon under laboratory conditions. According to their results, HFESQ seems to occur when annular two-phase flow pattern with significant droplet entrainment occurs (steam quality $X \geq 0.35$). It seems that the phenomenon is susceptible to the water chemistry (effect of amines) and size of the crud particles. However, this effect is not completely understood.

4.2.1.4 Adhesion of particles

Particles may or may not adhere to the surfaces, depending on the relative magnitudes of the chemical bond between the particle and the surface. This magnitude depends partly on liquid pH and the shear stress on the particle at the surface [49, 58, 59]. Sticking probability, S, can be used to describe the fraction of particles that adhere to the surface. When surface is clean and no perfect stickability is assumed Eq. 38 changes to Eq. 69.

$$\Phi_d = K_t C_b S = K_d C_b \quad (69)$$

There are some equations [49] that define the sticking probability. However, they are not giving information about the variables that have effect on the attachment process. The most important surface forces that have effect on the particle attachment are:

- London-van der Waals forces between particles and surface; these are attractive and dominate the gravity when $d_p \leq 100$ µm.
- Electrical double-layer interaction forces which are formed due to electric charges of particles and surfaces and the compensating diffuse layer at the surface. These forces can be attractive or repulsive.

Zeta-potential is the potential in the interfacial double layer (at the location of the slipping plane) of the particle versus a point in the bulk liquid located away from the surface of the particle. It can be related to colloidal stability and amount of repulsion or attraction between two surfaces. Ionic strength and pH have influence on zeta-potential values.

According to results of Barale et al., adhesion of magnetite, cobalt ferrite and nickel ferrite particles is favoured in the PWR primary side chemistry and temperature [60]. Surface charge of the magnetite particle is negative and adhesion on the walls depends on the surface charge of the construction materials. When London-van der Waals and electrical double-layer interactions are attractive, the deposition is controlled by the transport step. If surface forces are repulsive, the attachment step becomes limiting stage. The surface charge of alloy 690 (in PWR primary circuit) is positive and for ferrite alloys it is neutral or slightly negative. Adhesion of magnetite to these surfaces is favoured [60]. According to Basset et al., maximum deposition rate with magnetite particles was obtained at pH 7.5 most likely due to electrostatic interactions between wall and particle surfaces [55].

Klimas et al. and Turner et al. observed that amines have strong effect on the fouling behaviour [48, 61]. For example, when morpholine was used for alkalizing the fouling rate was 3-5 times higher than the in the case when the pH was controlled using dimethylamine. The rate of deposit removal was up to 5.5 faster than the rate of deposit consolidation when dimethylamine was used, whereas with morpholine the rate of consolidation was 6 to 20 times faster than the rate of removal. Barale et al. studied the effect of adsorption of lithium and borate species on the zeta potential of the particles of cobalt ferrite, nickel ferrite and magnetite (representing the corrosion products of primary circuit) at 25 °C and 70 °C [62]. According to their results, no effect of lithium was observed, whereas borate species cause a decrease of the isoelectric point (IEP).

The rate of particle deposition can decrease (autoretardation) when zeta-potential of the wall, flow velocity or heat flux changes due to deposition [49]. However, these effects have not been widely considered in the particle fouling models.

4.2.1.5 Consolidation

According to Lister et al., consolidation takes place in sub-cooled and bulk boiling conditions [47]. Consolidation is related to labile portion of the deposit according to Eq. 70.

$$m_{consolidation}(t) = m_{labile} * 10^{-4}\left(\frac{t}{t_c} - 1\right) \qquad (70)$$

Here m_{labile} is a function of the surface area of a nucleation site, active nucleation site density, heat flux and latent heat of vaporization and t_c is the critical time when consolidation first occurs.

Turner et al. studied steam generator sludge consolidation and made following conclusions based on their study [41]:

- Chemical reactions between sludge components and precipitation of feedwater impurities within existing sludge are important mechanisms of sludge consolidation.
- High ratio of copper (II) to copper (I) produces a hard sludge with a higher concentration of nickel ferrite.
- Sodium hydrogen phosphate increases the hardness of magnetite deposits.
- The formation of zinc silicate increases the hardness of sludge deposits.
- The precipitation of soluble impurities within the pores of sludge is an effective mechanism for sludge consolidation.

5 Conclusions

Magnetite dissolution and deposition are major problems in nuclear power plants. Mechanism of FAC is generally well-understood and there are several models and software that predict FAC rate with good accuracy. FAC can be considered as an extension of the general corrosion process where dissolution of the surface oxide is accelerated due to enhanced mass transfer of soluble species from the surface.

Main parameters that have influence on magnetite dissolution rate are concentrations of oxidants and reductants and electrochemical potential, temperature, pH, material properties (alloying elements) and hydrodynamic factors. FAC can occur at the various locations at the NPPs where carbon steel is used. Especially components that can promote the formation of vortices, secondary flows or turbulence are prone to FAC.

Factors affecting the magnetite deposition are basically less well understood. Theories of magnetite deposition can be separated to models describing the deposition of soluble iron or the deposition of magnetite particles. Soluble iron is deposited on the surfaces when temperature increases and solubility of the iron decreases. Water chemistry, (e.g. variables such as pH and ORP), also has an effect on the solubility of magnetite. Magnetite particles foul surfaces when they are transported on the surface by diffusion, inertia or impaction and attach on the surface. The formed deposit may consolidate after which its removal rate from the surface decreases. Especially factors affecting the attachment of particles on the surface should be studied further.

6 Summary

This work is a part of SAFIR2010, Finnish national research program on NPP safety 2007-2010. The goal of this review was to gather information from various sources to gain understanding of the present situation of the research related to magnetite dissolution and deposition.

Magnetite dissolution and deposition are major problems in many nuclear power plants (NPP). High removal rate of protecting oxide layer decreases the operating life of the equipment and causes dangerous situations, which can lead to casualties and major financial losses. Mechanism of flow accelerated corrosion (FAC) is generally well-understood and there are several models and software which predict FAC rate with good accuracy. FAC can be considered as an extension of the general corrosion process, where dissolution of the surface oxide is accelerated due to enhanced mass transfer of soluble species from the surface. The main parameters having influence on the magnetite dissolution rate are: concentrations of oxidants and reductants and electrochemical potential, temperature, pH, material properties (alloying elements) and hydrodynamic factors.

The factors affecting magnetite deposition are basically less well understood. Theories of magnetite deposition can be divided to models describing the deposition of soluble iron or the deposition of magnetite particles. Especially the factors affecting the attachment of the particles should be further studied.

References

1. Poulson, B., Complexities in predicting erosion corrosion, Wear 223-235 (1999) 497 - 504.
2. Odar, S., Nordmann, F., PWR and VVER Secondary System Water Chemistry - Stand Alone Report, A.N.T. International, Skultuna, Sweden, 2010.
3. Dooley, R. B., Chexal, V. K., Flow-accelerated corrosion of pressure vessels in fossil plants, Int. J. Press. Vessels Pip. 77 (2000) 85-90.
4. Jevec, J.M., Klimas, S.J., King, P., Fruzzetti, K., Multivariable Assessment of Flow Accelerated Corrosion and Steam Generator Fouling: Literature Review, EPRI, Palo Alto, CA: 2003. 1003619.
5. Dooley, R.B., Flow-Accelerated Corrosion in Fossil and Combined Cycle/HRSG Plants, Power Plant Chemistry, 10 (2008) 68-86.
6. Remy, F.N., Bouchacourt, M., Flow-assisted corrosion: a method to avoid damage, Nucl. Eng. Des. 133 (1992) 23-30.
7. Sanchez-Caldera, L. E., Griffith, P., Rabinowicz, E., The Mechanism of Corrosion-Erosion in Steam Extraction Lines of Power Stations, J. Eng. Gas Turbines Power 110 (1988) 180-184.
8. M. Bouchacourt, The impact of water chemistry on corrosion erosion in one phase and two phase flows, Proc. 5th Conf. on Water Chemistry, 1989.
9. M. Bouchacourt, Flow assisted corrosion of carbon steels in high temperature water: influence of water chemistry and mass transfer, proc. Conf. on Corrosion, UK, 1988.
10. Tremaine, P. R., LeBlanc, J. C., The Solubility of Magnetite and the Hydrolysis and Oxidation of Fe^{2+} in Water to 300 °C, J. Solution Chem. 9 (1980) 415-442.
11. Sweeton, F. H., Baes, C. F., The solubility of magnetite and hydrolysis of ferrous ion in aqueous solutions at elevated temperatures, J. Chem Thermodynamics 2 (1970) 479-500.
12. Thėbault, Y., Guibert, F., Moulart, P., Garnier, R., Calonne-Chatelee, V., The contribution of the metallurgical examinations to the FAC damage diagnostics, International FAC Conference on Flow Accelerated Corrosion, Lyon, France 2008.
13. Scottini, R., Wassink, C.H.P., Kooren, T., Condition assessment of components susceptible to Flow Accelerated Corrosion, International FAC Conference on Flow Accelerated Corrosion, Lyon, France 2008.
14. Findlan, S., Recommendations for an Effective Flow-Accelerated Corrosion Program (NSAC-202L-R3), EPRI Report TR-1015425, Palo Alto, CA, 2007.
15. Chexal, B., Flow Accelerated Corrosion in Power Plants, EPRI Report TR-106611-R1, Palo Alto, CA, 1998.
16. Kain, V., Roychowhdury, S., Mathew, T., Bhandakkar, A., Flow accelerated corrosion and its control measures for the secondary cycle pipelines in Indian power plants, J. Nucl. Mater., 383 (2008) 86-91.
17. Dooley, R.B., Shields, K. J., Cycle Chemistry for Conventional Fossil Plants and Combined Cycle/HRSGs, PowerPlant Chemistry, 2004 6(3), 53.
18. Dooley, R. B., Macdonald, D. D., Syrett, B. C., ORP - The Real Story for Fossil Power Plants, PowerPlant Chemistry, 2003 5(1), 5.
19. Davies, M. J., et al, Erosion Corrosion in AGR Boilers, Chimie 2002, Avignon, France, 2002.
20. PWR Secondary Water Chemistry Guidelines - Revision 5, EPRI Report TR-102134-R5, Palo Alto, CA, 2000.

21. Machiels, A., Munson, D., Chemistry Effects on Flow-Accelerated Corrosion - Pressurized Water Reactors: Hydrazine and Oxygen Investigations, EPRI Report TR-1011835, Palo Alto, CA, 2005.
22. Berge, P., Bouchacourt, M., Flow Accelerated Corrosion and Hydrazine, Eskom International Conference on Process Water Treatment and Power Plant Chemistry, Midrand, South Africa, November 1997.
23. Fruzzetti, K., Effect of Hydrazine on Flow Accelerated Corrosion, EPRI Report TR-1008208, Palo Alto, CA, 2005.
24. High temperature on-line monitoring of water chemistry and corrosion control in water cooled power reactors, Report of a co-ordinated research project 1995–1999, IAEA-TECDOC-1303, Vienna, Austria, 2002.
25. Dinov, K., Ishigure, K., Matsuura, C., Hiroishi, D., Solubility of magnetite in high temperature water and an approach to generalized solubility computations, J. Nucl. Mater. 207 (1993) 266-273.
26. Woolsey, I. S., Quirk, G., The use of oxygen to control flow accelerated corrosion, FAC2008 proceedings, Lyon 2008.
27. Cycle Chemistry Guidelines for Fossil Plants: Oxygenated Treatment, EPRI Report TR-102285, Palo Alto, CA, 1994.
28. Haag, J., Corrosion and redox potential measurements in German pressurized and boiling water reactors, Environmental Degradation of Materials in Nuclear Power Systems — Water Reactors (Proc. 8th Int. Symp.), ANS (1997) 632–640.
29. Pavageau, E.M., Michel, R., Influence of chemistry and temperature on the FAC rate of carbon steel: an example of study done at EDF R&D thanks to CIROCO loop, International FAC Conference on Flow Accelerated Corrosion, Lyon, France 2008.
30. Crockett, H. M., Horowitz, J. S., "Low Temperature" FAC, International FAC Conference on Flow Accelerated Corrosion, Lyon, France 2008.
31. Machiels, A., Crockett, H., Investigation into Flow-Accelerated Corrosion at Low Temperatures, EPRI Report TR-1013474, Palo Alto, CA, 2006.
32. Watanabe, Y., Hiroshi, A., Cr effect on FAC rate and its correlation with oxide layer characteristics, FAC2010 proceedings, Lyon 2010.
33. Jevec, J., King, P. J., Pearce, C. A., Fruzzetti, K., Sedman, K., Assessment of amine specific effects on the flow accelerated corrosion rate of carbon and low alloy steels, Proceedings of the 12th International Conference on Environmental Degradation of Materials in Nuclear Power Systems, Salt Lake City, Utah, USA 14-18 Aug. 2005.
34. King, P. J., Hua, F. H., Jevec, J. M., Pelger, R. H., Flow-accelerated Corrosion (FAC) Testing of Carbon and Low Alloy Steels in Nuclear Steam Generator Environments", Proceedings of the 4th International Steam Generator Conference, CNS, Toronto, May 2002.
35. Fukumura, T., Arioka, K., Influence of ethanol amine injection on FAC rate under simulated PWR secondary water, International FAC Conference on Flow Accelerated Corrosion, Lyon, France 2008.
36. Nasrazadani, S., Diaz, J., Stevens, J., Theimer, R., Effects of DBU, morpholine, and DMA on corrosion of low carbon steel exposed to steam, Corros. Sci. 49 (2007) 3024-3039.
37. Cubicciotti, D., Flow-assisted corrosion of steel and the influence of Cr and Cu additions, J. Nucl. Mater. 152 (1988) 259-264.
38. Machiels, A., Munson, D., Residual Chromium Effects on Flow-Accelerated Corrosion of Carbon Steel, EPRI Report TR-1011837, Palo Alto, CA, 2006.
39. Ducreux, J., Theoretical and experimental investigations of the effect of chemical composition of steels on their erosion-corrosion resistance, Specialists Meeting On Erosion-Corrosion on Steels in High Temperature Water and Wet Steam, Les Renardières, 1982.

40. Identification and Testing of Amines for Steam Generator Chemistry and Deposit Control, EPRI, Palo Alto, CA and Atomic Energy of Canada Limited, Chalk River, Ontario, Canada: 2002.1002773.
41. Turner, C. W., Blimkie, Lavoie, M. E. P.A., “Physical and Chemical Factors Affecting Sludge Consolidation,” Report AECL-11674/COG-96-492-1, Atomic Energy of Canada Ltd., Chalk River, Ontario (1997).
42. Tomlinson, L., Ashmore, C. B., Silver, P. J. B., Mead, A. P., The high temperature aqueous corrosion of ferritic steels: effect of heat flux on corrosion and magnetite deposition, Corrosion Science 30 (1990) 511-535.
43. Tomlinson, L., Hurdus, M. H., Ashmore, Silver, P. J. B., L., Sodium Heated Steam Generator Tubes: Effect of Heat Flux on the Deposition of Magnetite from Solution and Corrosion of the Underlying Steel, Corrosion 41 (1985) 257-264.
44. Kern, D. Q., Seaton, R. E., A theoretical analysis of thermal surface fouling, British Chemical Engineering, 4 (1959) 258-262.
45. Epstein, N., Particulate fouling of heat transfer surfaces: mechanisms and models, L. F. Melo (Eds.), Fouling Science and Technology, Kluwer Academic Publishers, Dordrecht, Netherlands, 1988.
46. Arbeau, N., Cook, W., Lister, D., The Early Stages of Deposition of Magnetite Particles onto Alloy-800 Heat Exchange Surfaces under Subcooled Boiling Conditions, Proceedings of 2003 ECI Conference on Heat Exchanger Fouling and Cleaning: Fundamentals and Applications, Santa Fe, USA.
47. Lister, D. H., Cussac, F. C., Modelling of particulate fouling on heat exchanger surfaces: influence of bubbles on iron oxide deposition, Proceedings of 7th International Conference on Heat Exchanger Fouling and Cleaning - Challenges and Opportunities, Tomar, Portugal, 2007.
48. Turner, C. W., Klimas, S. J., The effect of surface chemistry on particulate fouling under flow-boiling conditions, AECL-12171, Proceedings of Heat Exchanger Fouling: Fundamental Approaches and Technical Solutions, Davos, Switzerland, 2001.
49. Epstein, N., Elements of Particle Deposition onto Nonporous Solid Surfaces Parallel to Suspension Flows, Exp. Therm Fluid Sci.14 (1997) 323-334.
50. Cleaver, J. W., Yates, B., A Sublayer Model for the Deposition of Particles from a Turbulent Flow, Chem. Eng. Sci. 30 (1975) 983-992.
51. Johansen, S. T., The deposition of Particles on Vertical Walls, Int. J. Multiphase Flow 17 (1991) 355-376.
52. Papavergos, P. G., Hedley, A. B., Particle Deposition Behaviour from Turbulent Flows, Chem. Eng. Res. Design 62 (1984) 275-295.
53. Khumsa-ang, K., Lister, D. H., The investigation of particulate corrosion product deposition on heat transfer surfaces: a comparison of experimental and theory and a preliminary study of the removal mechanism, Proceedings of Heat Exchanger Fouling and Cleaning VIII - 2009, Schladming, Austria. 2009.
54. McNab, G. S., Meisen, A., Thermophoresis in liquids, J. Colloid Interface Sci. 44 (1973) 339-346.
55. Basset, M., McInerney, J., Arbeau, N., Lister, D. H., The Fouling of Alloy-800 Heat Exchange Surfaces by Magnetite Particles, Can. J. Chem. Eng. 78 (2000) 40-52.
56. Yung, B. P. K., Merry, H., Bott, T. R., The role of turbulent bursts in particle re-entrainment in aqueous systems, Chem. Eng. Sci. 44 (1989) 873-882.
57. Klimas, S. J., Pietralik, J. M., Fruzzetti, K., Tapping, R. L., Fouling Enhancement Under Flow Boiling At Elevated Steam Qualities, I. J. Trans. Phenomena. 6 (2004) 123-133.
58. Turner, C. W., Rates of partcile deposition from aqueous suspensions in turbulent flow: a comparison of theory with experiments, Chem. Eng. Sci. 48 (1993) 2189-2195.

59. Rummens, H. E. C., Rogers, J. T., Turner, C. W., The thermal hydraulics of tube support fouling in nuclear steam generators, Nucl. Technol. 148 (2004) 268-286.
60. Barale, M., Mansour, C., Carrette, F., Pavageau, E. M., Catalette, H., Lefèvre, G., Fadoroff, M., Cote, G., Characterization of the surface charge of oxide particles of PWR primary water circuits from 5 to 320 °C, J. Nucl. Mater. 381 (2008) 302-308.
61. Klimas, S. J., Fruzzetti, K., Turner, C. W., Balakrishnan, P. V., Strati, G. L., Tapping, R. L., Identification and Testing of Amines for Steam Generator Corrosion and Fouling Control, Proceedings of 2003 ECI Conference on Heat Exchanger Fouling and Cleaning: Fundamentals and Applications, Santa Fe, USA.
62. Barale, M., Lefèvre, G., Carrette, F., Catalette, H., Fédoroff, M., Cote, G., Effect of the adsorption of lithium and borate species on the zeta potential of particles of cobalt ferrite, nickel ferrite, and magnetite, J. Colloid Interface Sci. 328 (2008) 34-40.